

Article

Methodological Proposal for the Hydraulic Design of Labyrinth Weirs

Erick Dante Mattos-Villarroel¹, Waldo Ojeda-Bustamante^{2,*}, Carlos Díaz-Delgado³,
Humberto Salinas-Tapia³, Jorge Flores-Velázquez⁴ and Carlos Bautista Capetillo¹

¹ Campus Siglo XXI, Autonomous University of Zacatecas “Francisco García Salinas”, Road Zacatecas-Guadalajara Km 6, Zacatecas 98160, Mexico

² Research and Postgraduate Division, Chapingo Autonomous University, Chapingo, Texcoco 56230, Mexico

³ Inter-American Institute of Technology and Water Sciences, Autonomous University of the State of Mexico, Road Toluca-Atlaconulco Km 14.5, Toluca 50200, Mexico

⁴ Postgraduate College, Coordination of Hydrosocieties, Road Mexico- Texcoco Km 36.5, Texcoco 62550, Mexico

* Correspondence: w.ojeda@riego.mx

Abstract: A labyrinth weir allows for higher discharge capacity than conventional linear weirs, especially at low hydraulic heads. In fact, this is an alternative for the design or rehabilitation of spillways. It can even be used as a strategy in problems related to dam safety. A sequential design method for a labyrinth weir is based on optimal geometric parameters and the results of discharge flow analysis using Computational Fluid Dynamics and the experimental studies reported in the literature. The tests performed were for weirs with values of $H_T/P \leq 0.8$ and for angles of the cycle sidewall of $6^\circ \leq \alpha \leq 20^\circ$. The results of the discharge coefficient are presented as a family of curves, which indicates a higher discharge capacity when $H_T/P \leq 0.17$. Four aeration conditions are identified with higher discharge capacity when the nappe is adhering to the downstream face of the weir wall and lower discharge capacity when the nappe is drowned. Unstable flow was present when $12^\circ \leq \alpha \leq 20^\circ$, with a greater presence when the nappe was partially aerated and drowned. The interference of the nappe is characterized and quantified, reaching up to 60% of the length between the apex, and a family of curves is presented as a function of H_T/P in this respect. Finally, a spreadsheet and a flowchart are proposed to support the design of the labyrinth type weir.

Keywords: labyrinth weir; Computational Fluid Dynamics (CFD); spillways discharge capacity; spillway weir design



Citation: Mattos-Villarroel, E.D.; Ojeda-Bustamante, W.; Díaz-Delgado, C.; Salinas-Tapia, H.; Flores-Velázquez, J.; Bautista Capetillo, C. Methodological Proposal for the Hydraulic Design of Labyrinth Weirs. *Water* **2023**, *15*, 722. <https://doi.org/10.3390/w15040722>

Academic Editor: Diana De Padova

Received: 14 November 2022

Revised: 2 February 2023

Accepted: 5 February 2023

Published: 11 February 2023



Copyright: © 2023 by the authors. Licensee MDPI, Basel, Switzerland. This article is an open access article distributed under the terms and conditions of the Creative Commons Attribution (CC BY) license (<https://creativecommons.org/licenses/by/4.0/>).

1. Introduction

Labyrinth weirs are polygonal hydraulic structures (Figure 1) used to increase discharge capacity, for a fixed width, reducing hydraulic head relative to linear weirs. Their hydraulic performance characteristics make them an efficient and cost-effective alternative for spillway weir design or rehabilitation. This structure makes it possible to increase the storage volume in a reservoir and to control the water level. Figure 1 shows the geometrical parameters of a labyrinth weir, where W is the width of the channel (m), w is the width of the weir cycle (m), t_w is the width of the weir wall (m), D is the external length of the apex (m), A is the internal length of the apex (m), l_C is the length of the cycle sidewall (m), α is the angle of the cycle sidewall with respect to the flow direction ($^\circ$), B is the distance between apexes (m), P is the height of the weir (m), h is the piezometric head (m), H_T is the total head (m), and Q is the design flow ($\text{m}^3 \text{s}^{-1}$).

The design of a labyrinth weir is laborious because its discharge capacity is simultaneously affected by several factors, including the approach conditions and the geometry of the weir [2]. According to Bilhan, Emiroglu, and Miller (2016) [3], optimizing the geometry variables involved in the design of a labyrinth weir is an engineering challenge in which the following must be determined: (a) the configuration of the cycles, (b) the shape of the crest,

and (c) the orientation of the weir. For any type of weir, its geometry, particularly the shape of the crest profile, influences the value of the discharge coefficient. Willmore (2004) [4] indicated that half-round crest profiles are more efficient than sharp-crest and quarter-round profiles, because they allow the nappe to remain adhered to the wall of the structure for small heads. Typically, the cycle's apex facilitates the concrete construction of a labyrinth weir. From a hydraulic perspective, a labyrinth weir with a smooth upstream transition is relatively more efficient than the abrupt transition presented by a trapezoidal labyrinth weir [5]. In this regard, Tullis and Young (2005) [6] reported an increase in discharge efficiency at Brazos Dam (Wako, TX, USA) by creating a smooth transition between the flow and the circular apices of the labyrinth spillway cycles.

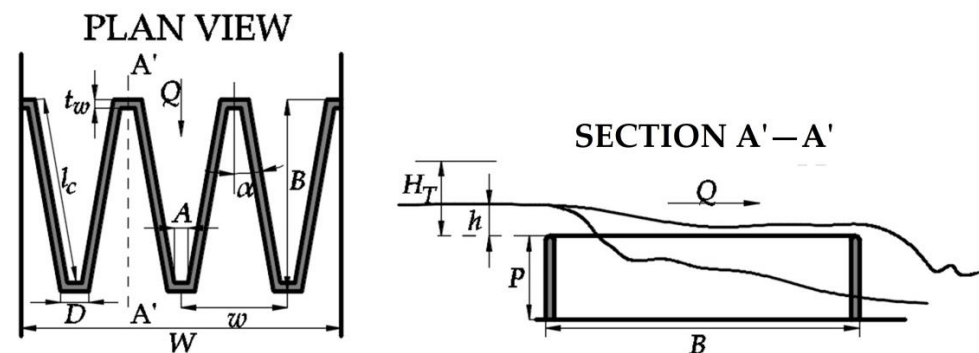


Figure 1. Geometric parameters of a labyrinth type weir (Mattos-Villaruel et al., 2021 [1]).

Families of discharge coefficient curves (C_d) for the design of labyrinth weirs have been determined from physical models of various prototype structures, examples of which are as follows: Avon and Woronova [2]; Harrezza, Dungo, Keddara, Alijó, Gema, and São Domingo [7]; Hyrum [8]; Ute [9]; Lake Brazos [6]; and Lake Townsend [10]. The evolution of commonly used and documented design methods can be summarized in the following sequence: (a) Hay and Taylor (1970) [11]; (b) Darvas (1971) [2]; (c) Hinchliff and Houston (1984) [12]; (d) Lux (1989) [13]; (e) Magalhães and Lorena (1989) [7]; (f) Tullis, Amanian, and Waldron (1995) [14]; and (g) Crookston and Tullis (2012) [15]. However, the results of Idrees and Al-Ameri (2022) [16] showed that common design equations did not take into account all the parameters that affect the performance of a labyrinth weir such as geometry and flow conditions.

On the other hand, physical and numerical modeling are used as complementary tools to improve the design of hydraulic structures. Indeed, Computational Fluid Dynamics (CFD) makes it possible to obtain, by means of numerical techniques, adequate results for the equations that predict the behavior of any flow. In general, the equations to be solved with CFD are the Navier–Stokes equations. Thus, numerical modeling facilitates the hydraulic evaluation of structures, such as weirs, to obtain information on pressure fields and velocities under different geometric and hydraulic conditions. It is important to highlight the use of CFD as a tool in the generation of information to support decision-making and the design of hydraulic structures. In particular, the performance of CFD in the modeling of flow over linear weirs, particularly the labyrinth type, stands out, as has been demonstrated by several researchers [1,17–22]. Ben Said et al. (2022) [23] using CFD proved that the discharge capacity of a labyrinth weir can increase as its downstream channel bed level decreases. Samadi et al. (2022) [24] experimentally and numerically investigated the effects of geometric parameters on the efficiency in triangular and trapezoidal labyrinth weirs.

1.1. Discharge Flow Characteristics

The behavior and characteristics of the discharge flow presented by the complex geometry of the labyrinth weir must be considered in its hydraulic analysis and design. This analysis must consider the aeration conditions, the instability of the discharge flow,

and the collision between the nappes that occurs between the walls of the weir cycles. It should be noted that each of these factors individually affects the value of the discharge coefficient C_d and the efficiency of the weir. However, the main challenge is to know the joint effect of all these factors on the discharge coefficient.

1.1.1. Aeration Conditions

The efficiency and discharge capacity of the labyrinth weir also depends on the aeration regime of the nappe, which is influenced by the shape of the crest, the level of the hydraulic head, the height of the weir, the flow path over the crest, the turbulence, and the pressure under the nappe.

The increase in discharge flow over the weir generates different aeration conditions; these have been identified by some researchers and have already been included in design curves, through the value of the discharge coefficient [25,26]. Lux and Hinchliff (1985) [25] identified three types of aeration: aerated, transitional (partially aerated), and suppressed (drowned). However, for Falvey (2003) [27], there are four types of aeration conditions: cavity, atmospheric, sub-atmospheric, and pressure. On the other hand, Crookston and Tullis (2012) [26] also reported four types of aeration: clinging, aerated, partially aerated, and drowned, and indicated that aeration conditions can produce pressure fluctuations at the sidewalls of the weir, low frequency sound, and vibrations. In addition, previous studies point to the labyrinth weir as an excellent aeration control structure. Examples of this are the work of Hauser (1996) [28], who describes the methods for the design of this type of weir, taking into consideration the aeration conditions during discharge. Wormleaton and Soufani (1998) [29] and Wormleaton and Tsan (2000) [30] found that a rectangular labyrinth weir has better aeration efficiency than a triangular labyrinth weir and that the latter is better than a linear one.

1.1.2. Nappe Instability

Under certain flow conditions and weir geometry, the nappe becomes unstable, and vibrations occur in the hydraulic structure. Several researchers have conducted studies on nappe instability. Crookston and Tullis (2012) [26] defined nappe instability as a nappe with an oscillating trajectory. These authors, supported by experimental observations, reported that the flow streamlines under this condition are helical, adjacent, and parallel to the weir walls. Furthermore, these nappes occur momentarily with changes of aeration condition, most frequently during the aerated and partially aerated condition, when their presence causes vibrations that threaten the safety of the structure. It is recommended that these conditions should be considered during the design of the weir and are to be avoided. According to Casperson (1995) [31], vibrations are easily felt by touch and the sound can be heard over a kilometer away. For Naudascher and Rockwell (2017) [32], the vibrations are attributed to inadequate aeration below the discharge flow and indicate that an unventilated air pocket behind the nappe can amplify the instability of the weir. Similarly, according to their research, the three-dimensional characteristic of the flow during discharge, at the point of detachment and the height of fall, may be a significant parameter in the presence of vibrations. Falvey (2003) [27] even pointed out that the vibration of the nappe occurs when the weir operates at low hydraulic heads, in the range $0.01 \leq h/P \leq 0.06$.

Some researchers recommend the use of splitters, placed vertically and normal to the flow to reduce vibrations [12,33]. However, because several splitters are required, this solution was not recommended by Falvey (2003) [27]. To eliminate vibrations, the Metropolitan Water, Sewerage, and Drainage Board (1980) [34] conducted studies on a physical model of the Avon Dam, located in Australia, where they increased the crest roughness. However, with only a 15 mm increase in crest height, the discharge decreased by 2%.

1.1.3. Nappe Interference

Nappe interference refers to the collision between nappes at the upstream apexes of the weir. This hydraulic phenomenon decreases the efficiency of the weir. The length of

the interference depends on the width apex, the shape of the crest, the weir height, the hydraulic head, and the aeration conditions.

Indlekofer and Rouve (1975) [35] studied the nappe interference in single-cycle triangular weirs whose sidewalls are perpendicular to the channel walls, also known as corner weirs. These authors identified a perturbed region, where the nappes from each weir sidewall collide, and a second region, where streamlines are perpendicular to the weir wall, similar to the discharge over a linear weir. Finally, they found an empirical relationship between the average discharge coefficient of the disturbed area, the theoretical crest length of the disturbed region, and the discharge to compare the efficiency of a corner weir with a linear weir. Lux (1989) [13] recommended that the ratio of the apex width to the weir cycle width should be less than 0.0765, so that the effects of the collisions of the nappes do not generate large reductions in the performance of the trapezoidal labyrinth weir. Falvey (2003) [27] developed an empirical model that considered the data relationship of Indlekofer and Rouve (1975) [35], and then developed a second equation based on the analysis of experimental data from a labyrinth weir. However, this author did not indicate which of the two proposed equations was the most appropriate, but the significant influence of the nappe interference on aeration in triangular labyrinth weirs was highlighted.

Based on the quantity of movement, Osuna 2000 [36] analyzed the hydraulic behavior of a weir, located inside a channel and oblique to the upstream flow direction, and proposed an equation that allows for the calculation of the flow per unit length of the weir. The results indicated that the direction of flow at the outlet of the weir depends on the ratio of the thickness of the nappe contracted over the weir and the height of free-surface water, upstream from a point sufficiently far from the weir. In the last decade, Granell and Toledo (2010) [37] adapted the mathematical model of Osuna (2000) [36] to labyrinth weirs in order to obtain the nappe's collision length.

1.1.4. Drowning

It has been observed that the drowning phenomenon in labyrinth weirs has a behavior similar to that in the operation of linear weirs [38]. However, Taylor (1968) [39] concluded that drowning effects are less significant for labyrinth weirs than for linear weirs.

The linear weir drowning analysis developed by Villemonte (1947) [40] was the most applied method for labyrinth weirs under drowning conditions. However, at the beginning of the century, Tullis et al. (2007) [38] developed a dimensionless relationship for drowning heads in labyrinth weirs, obtaining an average error of up to 0.9%. Figure 2 shows the function describing drowning at the weir, which was divided into three sections to better explain its behavior and is represented by Equations (1)–(3).

$$\frac{H^*}{H_T} = 0.3320 \left(\frac{H_d}{H_T} \right)^4 + 0.2008 \left(\frac{H_d}{H_T} \right)^2 + 1; 0 \leq \frac{H_d}{H_T} \leq 1.53 \quad (1)$$

$$\frac{H^*}{H_T} = 0.9379 \frac{H_d}{H_T} + 0.2174; 1.53 \leq \frac{H_d}{H_T} \leq 3.5 \quad (2)$$

$$H^* = H_d; 3.5 \leq \frac{H_d}{H_T} \quad (3)$$

H^* is the upstream total head when the weir is drowned (m), H_T is the upstream total head when the weir is not drowned (m), and H_d is the downstream total head of the weir in the drowning state (m).

Based on the above, and due to the complexity in the hydraulic analysis of a labyrinth weir, the objective of this work is focused on proposing a sequential design that facilitates the conception of a labyrinth weir, based on the results of numerical modeling in CFD and by considering the relationships between the geometric variables of the weir and the simultaneous effect of the hydraulic phenomena that occur on the nappe.

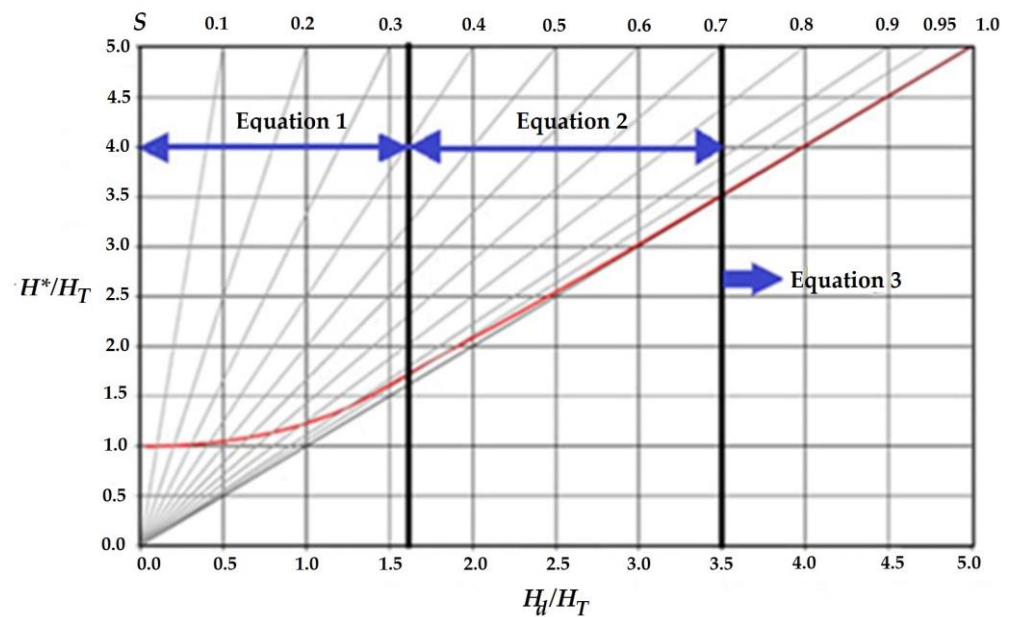


Figure 2. Submergence limits (adapted from Tullis et al., 2007 [38]).

2. Materials and Methods

2.1. Description of the Physical Model

The construction of the conceptual model and its evaluation in CFD are based on the experimental prototype reported by Crookston and Tullis (2012) [15]. The physical model consisted of a trapezoidal labyrinth weir with a quarter-round crest profile made of high-density polyethylene, located within a rectangular channel. The description of the dimensions and geometric characteristics of the labyrinth weir are specified in Table 1.

Table 1. Geometric characteristics of the trapezoidal labyrinth weir [15].

α (°)	N	L (m)	A (m)	w (m)	P (m)	W (m)	Crest Profile
15	2	4	0.038	0.617	0.305	1.235	Quarter-round

2.2. Numerical Solution Method

2.2.1. Computational Fluid Dynamics (CFD)

Numerical modeling was performed using the ANSYS-FLUENT simulation software [41,42]. This software is considered to be a general purpose CFD code, which has been widely used in recent years, due to the advancement of technology, mainly computational technology. ANSYS-FLUENT allows for the modeling of flows in one phase to flows in multiple phases (multiphase) in both closed and open domains. The numerical simulation was performed with two-phase flow models, incompressible conditions, and a free-surface interface.

ANSYS-FLUENT implements the approach to surface analysis using the volume of fluid (VOF) scheme. The VOF scheme is ideal for applications involving free-surface flows. It involves defining a volume fraction function for each of the fluids in the entire domain.

The governing equations for all fluid fractions were solved using the two-phase (air-water) flow model. A two-phase flow model was used to detect under pressure; air inertia and air-water interaction effects were neglected in the numerical model. The VOF method was used to improve the accuracy of the free-surface simulations.

For incompressible fluids, when the density of water is constant, the mass continuity equation of motion of the fluid in Cartesian coordinates is given as Equation (4) [43]:

$$\frac{\partial}{\partial x}(uA_x) + \frac{\partial}{\partial y}(vA_y) + \frac{\partial}{\partial z}(wA_z) = 0. \tag{4}$$

where $A_x, A_y,$ and A_z are the fractional areas open to the fluid in directions $x, y,$ and $z,$ respectively. Additionally, $u, v,$ and w are the velocity components in the directions $x, y,$ and $z,$ respectively.

The Navier–Stokes equations, with the velocity components as momentum equations, are used to determine the 3D fluid motion in Cartesian coordinates (Equations (5)–(7)) [43].

$$\frac{\partial u}{\partial t} + \frac{1}{V_F} \left[uA_x \frac{\partial u}{\partial x} + vA_y \frac{\partial u}{\partial y} + wA_z \frac{\partial u}{\partial z} \right] = -\frac{1}{\rho} \frac{\partial(p)}{\partial y} + G_x + f_x \tag{5}$$

$$\frac{\partial v}{\partial t} + \frac{1}{V_F} \left[uA_x \frac{\partial v}{\partial x} + vA_y \frac{\partial v}{\partial y} + wA_z \frac{\partial v}{\partial z} \right] = -\frac{1}{\rho} \frac{\partial(p)}{\partial y} + G_y + f_y \tag{6}$$

$$\frac{\partial w}{\partial t} + \frac{1}{V_F} \left[uA_x \frac{\partial w}{\partial x} + vA_y \frac{\partial w}{\partial y} + wA_z \frac{\partial w}{\partial z} \right] = -\frac{1}{\rho} \frac{\partial(p)}{\partial z} + G_z + f_z \tag{7}$$

where V_F is the fraction volume open to the fluid; $G_x, G_y,$ and G_z are the acceleration components of the body, and $f_x, f_y,$ and f_z are the viscous acceleration components in the directions $x, y,$ and $z,$ respectively.

To define fluid configurations, the volume of fluid function (VOF) represents a volume of fluid per unit volume [44], as indicated in Equation (8):

$$\frac{\partial F}{\partial t} + \frac{1}{V_F} \left[\frac{\partial}{\partial x}(FA_x u) + \frac{\partial}{\partial y}(FA_y v) + \frac{\partial}{\partial z}(FA_z w) + \varphi \frac{FA_x u}{x} \right] = F_D + F_S \tag{8}$$

where F_D is the diffusion term, applied only in the turbulent mixture of a two-phase flow, and F_S is a source term.

To determine the discharge and pressure characterization at the weir crest, the two-phase model (air and water) was applied. In addition, the standard $k-\epsilon$ model was used to analyze the effects of turbulence, which solves two transport equations with Reynolds stresses for the turbulent kinetic energy (k) and the dissipation rate (ϵ). The $k-\epsilon$ turbulence model is a semi-empirical model with low computational cost; several researchers have demonstrated its advantages and excellent results for the simulation of confined, internal, and free-surface flows [19,43,45–47].

Equations (9) and (10) were used to obtain the turbulent kinetic energy and dissipation rate. The $k-\epsilon$ model is described below [48].

$$\frac{\partial k}{\partial t} + \frac{\partial k u_i}{\partial x_i} = \frac{\partial}{\partial x_i} \left(Dk_{eff} \frac{\partial k}{\partial x_i} \right) + G_k - \epsilon \tag{9}$$

$$\frac{\partial \epsilon}{\partial t} + \frac{\partial \epsilon u_i}{\partial x_i} = \frac{\partial}{\partial x_i} \left(D\epsilon_{eff} \frac{\partial \epsilon}{\partial x_i} \right) + C_{1\epsilon} \frac{\epsilon}{k} G_k - C_{2\epsilon} \frac{\epsilon^2}{k} \tag{10}$$

where G_k is the generation of turbulent kinetic energy due to mean velocity gradients; DDk_{eff} and $D\epsilon_{eff}$ are the effective diffusivity for the turbulent kinetic energy (k) and the dissipation rate (ϵ), respectively, determined by Equations (11) and (12):

$$Dk_{eff} = \nu + \nu_t \tag{11}$$

$$D\epsilon_{eff} = \nu + \frac{\nu_t}{\sigma_\epsilon} \tag{12}$$

where $\nu_t = C_\mu \frac{k^2}{\epsilon}$ is the turbulent kinematic viscosity at each point; σ_ϵ is the Prandtl number for ϵ and takes the value 1.3; and the constants $C_{1\epsilon}, C_{2\epsilon},$ and C_μ have values of 1.44, 1.92, and 0.09, respectively. $G_k = 2\nu_t S_{ij}^2$ is the turbulent kinetic energy result, and S_{ij}^2 is the strain rate tensor.

For the solution of the equations, the Semi-Implicit Method for Pressure Linkek Equations (SIMPLE) algorithm was used, which approaches convergence through a series of intermediate pressure and velocity fields satisfying continuity [49]. The higher order

Upwind spatial discretization system was also used, which ensures stable schemes by minimizing numerical diffusion errors [49]. Both schemes are integrated in ANSYS-FLUENT.

The ANSYS-FLUENT *Geometry* module was used to build the conceptual models. The *Meshing* module was used to generate the mesh, where they were spatially discretized using predominantly hexahedral meshes. The advantage of this type of mesh is the reduction in the number of cells and the improvement in the convergence of the solution [50]. The computational meshes were refined in the vicinity of the weir wall (Figure 3B), where the turbulence is dissipated, and its behavior has a significant effect on the results.

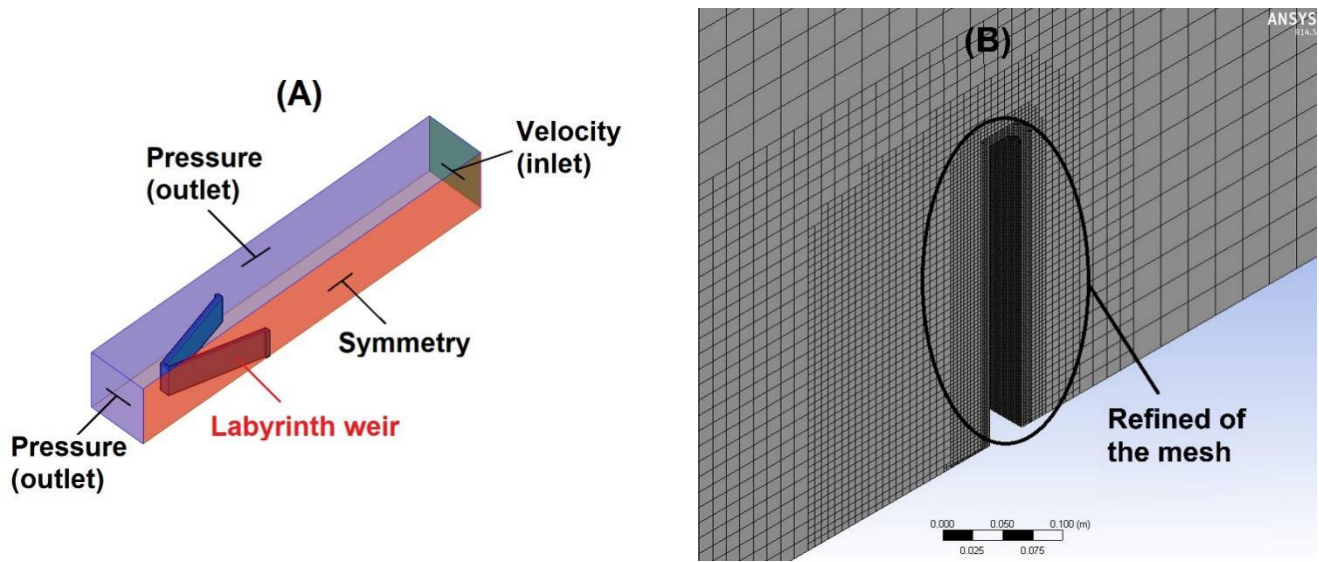


Figure 3. (A) Boundary conditions (Mattos-Villarroel et al., 2021 [1]). (B) Refined mesh.

In the simulation of free-surface flows, it is important to define the boundary conditions appropriately at the inlet and outlet of the model domain. In this work, the boundary conditions implemented in ANSYS-FLUENT were applied at the inlet and outlet of the domain, with the fluid velocity as inlet and atmospheric pressure as outlet. The approach of the boundary conditions (Figure 3A) and definition of the fluid properties are specified in Table 2.

Table 2. Boundary and initial conditions.

Boundary and Initial Conditions	Solution Method
Domain: inlet	Velocity
Domain: outlet	Atmospheric pressure
Domain: weir, sidewalls, and channel platform	Solid, stationary, and non-slip.
Viscosity model	$k-\epsilon$ standard
Multiphasic model	Volume of fluid (VOF)
Pressure–velocity coupling	SIMPLE
Spatial discretization scheme	Upwind

2.2.2. Grid Convergence Index (GCI)

Within the simulation, the shape and density of the mesh or grid in the analysis have a very significant importance and influence the total number of elements, the computing time, and the accuracy of the analysis. In the present study, 40 different scenarios with 7 grid sizes of different densities were analyzed (Table 3). In each grid, the number of elements was decreased until we obtained an adequate convergence of calculations, and the independence results of the mesh were obtained.

Table 3. Simulated scenarios for each grid.

Grid	Scenario	Grid	Scenario
I	1–10	V	26–30
II	11–15	VI	31–35
III	16–20	VII	36–40
IV	21–25		

It is important that, before calculating any discretization error estimate, it must be guaranteed that the convergence of the iterative process presents a decrease of at least three orders of magnitude in the normalized residuals for each solved equation [51]. In the present study, the convergence and discretization errors were verified at each time step to control the convergence of the solution of the time-dependent problems and, thereby, guarantee an adequate solution to the equations describing the phenomenon.

The recommended method for discretization error estimation is the Richardson extrapolation method. Roache (1994) [52] proposed a way of reporting the results of grid convergence studies with the Grid Convergence Index (GCI), which is based on the Richardson Extrapolation method, a method that has been extensively evaluated in case studies using CFD [51,53,54]. GCI indicates the percentage by which the calculated value deviates from the asymptotic numerical value and how much the solution would change with further refinement of the mesh. Thus, a small value of GCI indicates that the calculation is within the asymptotic range [55]. To estimate the order of convergence and verify that the solutions are within the asymptotic range of convergence, Roache (1994) [52] recommended using three different grid sizes.

Equation (13) shows how to determine the CGI of a fine or coarse grid [56]:

$$GCI_{fine} = \frac{F_s |\epsilon_{i+1,1}|}{(r^p - 1)}; GCI_{coarse} = \frac{F_s |\epsilon_{i+1,1}| r^p}{(r^p - 1)} \quad (13)$$

where F_s is a security factor (taking a value of 3 for comparisons of two grids and 1.25 for comparisons of three or more grids [56]), r is the mesh refinement ratio, p is the order of convergence, and ϵ is the error relative to the control variable f_i .

The representative model cell size (λ) was estimated using Equation (14) for three-dimensional models.

$$\lambda = \left[\frac{1}{N_C} \sum_{i=1}^N (\Delta V_i) \right]^{\frac{1}{3}} \quad (14)$$

In this equation, ΔV_i is the volume of the i -th cell and N_C is the number of cells. Therefore, to perform the calculation, at least three different grid sizes must be selected to determine the value of the control variables $f_i (f_1, f_2, f_3)$ considered important for the simulation objective. Then, for $\lambda_1 < \lambda_2 < \lambda_3$, the mesh refinement factors were determined as $r_{21} = \lambda_2/\lambda_1$, $r_{32} = \lambda_3/\lambda_2$ and the order of convergence p was calculated with Equation (15) [52].

$$p = \frac{\ln \frac{f_3 - f_2}{f_2 - f_1}}{\ln r} \quad (15)$$

Equation (16) enables verification that the solutions are within the asymptotic range of convergence [55]:

$$\frac{GCI_{23}}{GCI_{12} r^p} \approx 1 \quad (16)$$

Seven different grids are presented in this study. To perform the GCI analysis, the hydraulic head (h_1, h_2, h_3) was considered as a control variable to estimate discretization errors. The flows used were as follows: $Q_I = 0.2036 \text{ m}^3 \text{ s}^{-1}$, $Q_{II} = 0.2003 \text{ m}^3 \text{ s}^{-1}$, $Q_{III} = 0.2137 \text{ m}^3 \text{ s}^{-1}$, $Q_{IV} = 0.2170 \text{ m}^3 \text{ s}^{-1}$, $Q_V = 0.2149 \text{ m}^3 \text{ s}^{-1}$, $Q_{VI} = 0.2036 \text{ m}^3 \text{ s}^{-1}$, and $Q_{VII} = 0.1915 \text{ m}^3 \text{ s}^{-1}$ for the grids: I, II, III, IV, V, VI, and VII, respectively. The GCI cal-

culations of the numerical solutions are summarized in Table 4; the asymptotic ranges of convergence obtained are approximately equal to 1. Therefore, the numerical solutions are within the asymptotic range. In the present work, the hydraulic head was achieved with a maximum error of up to 2.80%, corresponding to grid II.

Table 4. Estimation of grid convergence index (CGI).

Grid	r	p	h_1 (m)	h_2 (m)	h_3 (m)	Richardson Extrapolate (m)	ϵ_{21}	ϵ_{32}	GCI ₂₁ (%)	GCI ₃₂ (%)	Asymptotic Range of Convergence
I	1.60	1.80	0.1622	0.1637	0.1672	0.1611	0.0092	0.0214	0.87	2.00	0.99
II	1.58	1.78	0.1182	0.1197	0.1231	0.1170	0.0127	0.0284	1.25	2.80	0.99
III	1.58	1.83	0.1302	0.1312	0.1335	0.1294	0.0077	0.0175	0.74	1.69	0.99
IV	1.59	1.76	0.1412	0.1423	0.1448	0.1403	0.0078	0.0176	0.77	1.73	0.99
V	1.65	1.79	0.1482	0.1495	0.1527	0.1473	0.0088	0.0214	0.75	1.83	0.99
VI	1.58	1.97	0.1502	0.1519	0.1561	0.1490	0.0113	0.0276	0.96	2.35	0.99
VII	1.64	1.89	0.1622	0.1631	0.1654	0.1616	0.0055	0.0141	0.45	1.13	0.99

Based on Richardson’s extrapolation for the two finer grids, an estimate of the hydraulic head value for zero-grid spacing was obtained. The graph in Figure 4 shows the hydraulic head with variable grid spacing; as the grid spacing reduced, the hydraulic head approached an asymptotic value of zero mesh spacing.

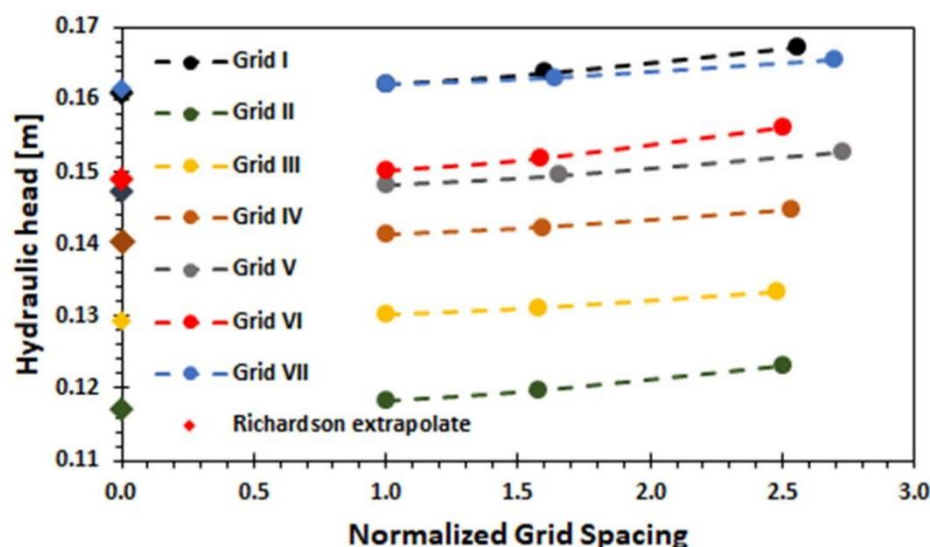


Figure 4. Hydraulic head approaching an asymptotic zero-grid spacing value.

2.3. Evaluation of the Computational Model

Numerically, 40 scenarios were modeled. Table 5 details the design flow applied and the geometric characteristics of the simulated weirs for each scenario.

For the evaluation of the computational model, the results of the numerically obtained discharge coefficient were compared with the experimental values reported by Crookston and Tullis (2012) [15], corresponding to scenarios 1–10. The discharge coefficient (C_d) was calculated from the height of the measured hydraulic head on the weir and the general weir equation (Equation (17)).

$$Q = \frac{2}{3} \sqrt{2g} C_d L H_T^{3/2} \tag{17}$$

where Q is the design flow ($\text{m}^3 \text{s}^{-1}$), C_d is the discharge coefficient (dimensionless), g is the acceleration due to gravity (m s^{-2}), L is the characteristic length of the weir (m) (defined as the total length referenced at the center of the weir crest wall thickness), and H_T is the total hydraulic head (m).

Table 5. Simulation scenarios for labyrinth weirs.

Scenario	α (°)	P (m)	L_{cycle} (m)	w/P	N	Q ($m^3 s^{-1}$)	Crest Profile	Apex Shape
1, 2, 3, 4, 5, 6, 7, 8, 9, 10	15	0.305	2.00	2.024	1	0.0190, 0.0532, 0.0919, 0.1309, 0.1681, 0.2036, 0.2373, 0.2697, 0.3013, 0.3325	CR	Trapezoidal
11, 12, 13, 14, 15	6	0.305	3.64	2.024	1	0.0780, 0.1240, 0.2003, 0.2703, 0.3558	MR	Circular
16, 17, 18, 19, 20	8	0.305	3.07	2.024	1	0.0429, 0.0750, 0.2137, 0.2873, 0.3744	MR	Circular
21, 21, 23, 24, 25	10	0.305	2.65	2.024	1	0.0367, 0.0532, 0.2170, 0.2891, 0.3712	MR	Circular
26, 27, 28, 29, 30	12	0.305	2.33	2.024	1	0.0380, 0.0671, 0.1450, 0.2149, 0.3728	MR	Circular
31, 32, 33, 34, 35	15	0.305	2.02	2.024	1	0.0532, 0.1308, 0.2036, 0.2697, 0.3325	MR	Circular
36, 37, 38, 39, 40	20	0.305	1.59	2.024	1	0.0290, 0.0517, 0.1247, 0.1915, 0.3364	MR	Circular

Note: CR: Quarter-round; MR: Half-round; L_{cycle} : Cycle length (m).

Statistical criteria were applied to evaluate the performance of the model, such as Pearson’s coefficient of determination (R^2), the relative percentage error (Er), and the mean absolute error (MAE) (Equations (18)–(20)). These criteria assess the agreement between the results of the physical experiment and those from the CFD models.

$$R^2 = \frac{Cov(num, exp)^2}{\sigma_{num}^2 \sigma_{exp}^2} \tag{18}$$

$$MAE = \frac{\sum_i^n |Y_{num,i} - Y_{exp,i}|}{n} \tag{19}$$

$$Er(\%) = \frac{|Y_{num} - Y_{exp}|}{Y_{exp}} * 100 \tag{20}$$

$Cov(num, exp)$ is the covariance of the numerical and experimental results, σ_{exp}^2 is the variance of the experimental results, σ_{num}^2 is the variance of the numerical results, Y_{num} are the numerical values, and Y_{exp} are the experimental values.

The mean absolute error of the discharge coefficient (MAE) was 0.0128, and the relative percentage error varied from 1.89% to 4.92%. In Figure 5, the relative percentage errors of the discharge coefficient as a function of the ratio H_T/P are presented.

The calculated coefficient of determination was $R^2 = 0.984$, which confirms the agreement between the numerically obtained discharge coefficients and the experimental values. In the graph in Figure 6, the numerical results are compared with the experimental results; the dotted diagonal line corresponds to a perfect fit.

In this study, the ANOVA statistical analysis was performed, and there was no significant difference between the discharges coefficients obtained numerically and experimentally for a significance level of 5% (0.05).

2.4. Proposed Sequential Design Method for a Labyrinth Weir

Figure 7 details the variables and geometric characteristics considered in the proposed sequential design method for the labyrinth weir.

The design method is basically subdivided into four stages: (i) initial data requirements, (ii) definition of the number of cycles and the angle α to make the weir hydraulically efficient, (iii) calculation of the geometric variables, and (iv) analysis of the submerged weir developed according to Tullis et al., (2007) [38].

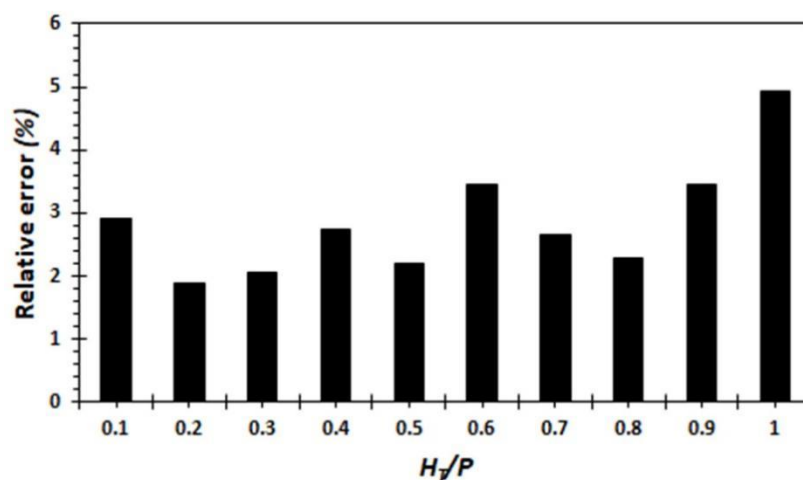


Figure 5. Relative percentage error of the discharge coefficient as a function of H_T/P (Mattos-Villaruel et al., 2021 [1]).

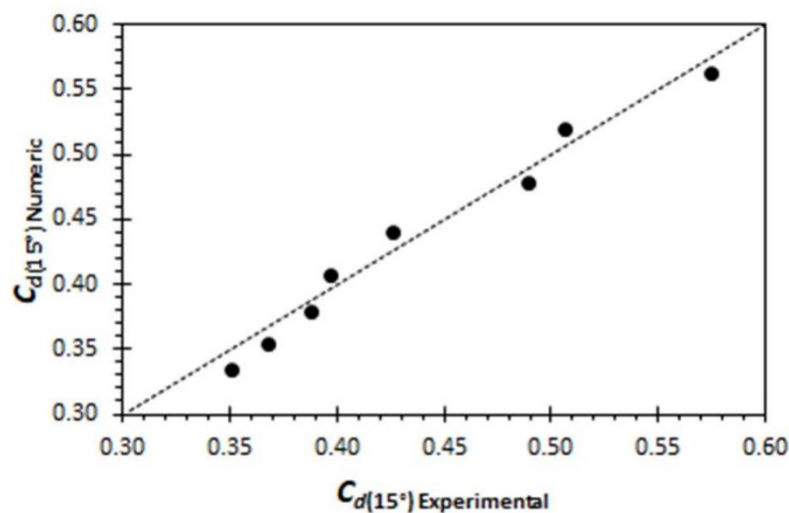


Figure 6. Comparison of numerically obtained discharge coefficients with experimental values (Mattos-Villaruel et al., 2021 [1]).

(i) Stage one: This stage consists of determining the data necessary for the design and comprises information previously obtained from topographic and hydrological analysis, namely:

- The design flow (Q), which represents the design discharge for a given return period;
- The upstream head of the weir (H_T), which depends on the channel width (W) and is limited by the freeboard;
- The downstream head of the weir (H_d) is calculated from the drop height and the flow velocity at the foot of the weir;
- The weir height (P) corresponds to the height of the storage volume or the Ordinary Maximum Water Level obtained from the topography and the operation of the basin.

The width of the weir or the channel (W) is generally restricted by the topography of the study area.

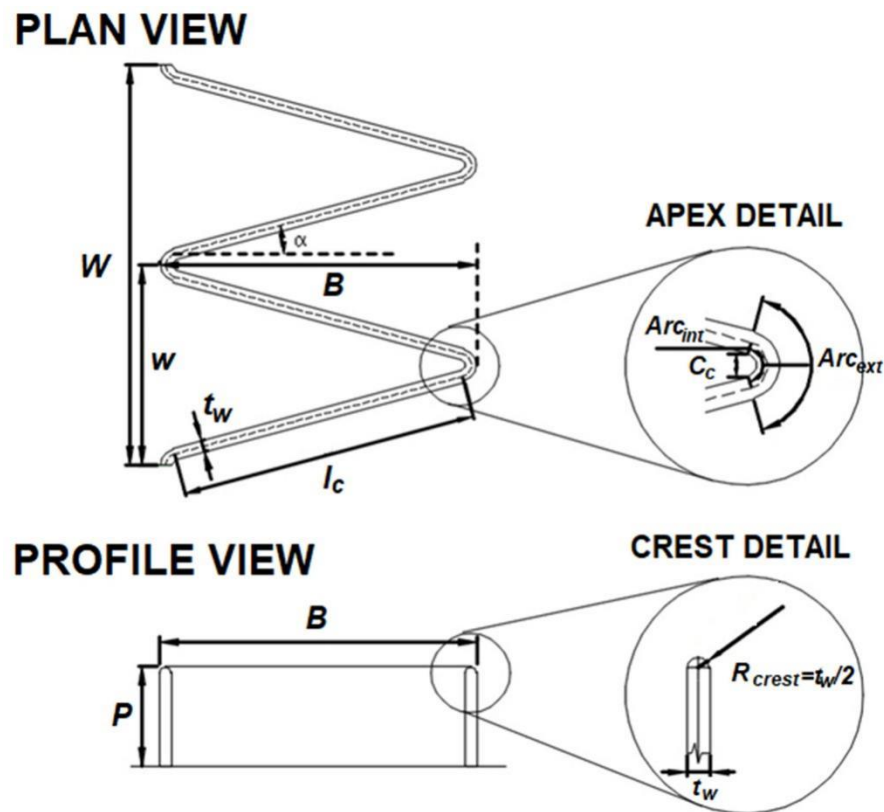


Figure 7. Geometric variables of a labyrinth weir.

(ii) Stage two: The topography of the study area allows for selecting the angle α of the weir sidewall ($6 \leq \alpha \leq 20^\circ$). A large angle can be chosen when the number of cycles N and the length between the cycle apexes (B) are limited by topography. The selection of the angle α is also a function of the ratio H_T/P ($0.05 \leq H_T/P \leq 0.8$). For certain values of H_T/P and α , the flow becomes unstable and is a phenomenon to be avoided in the design of the weir, for the safety of the hydraulic structure. Subsequently, the discharge coefficient is calculated. Its calculation is a function of α and the ratio H_T/P , and the value of the discharge coefficient will determine the discharge capacity of the weir.

Then, the cycle width w is calculated as a function of the weir height P . For Taylor (1968) [39], the ratio w/P (known as the vertical aspect) should not be less than 2 because it would contribute to reducing weir efficiency. On the other hand, Tullis et al. (1995) [14] recommended that w/P should not be greater than 4. Considering both criteria, it is recommended that the ratio w/P should be equal to 3 or, in other words, the cycle width w should be 3 times the weir height P , to ensure that the weir is hydraulically efficient.

Another important variable influencing the design is the number of cycles (N). The number of cycles is calculated as the ratio of the weir width (W) to the cycle width (w). For ease of design, it is recommended that this be a multiple of 0.5, and so the cycle width should be recalculated as $w = W/N$, with the restriction that the ratio w/P is within the range $2 \leq w/P \leq 4$.

(iii) Stage three: In this stage, the geometric variables of the weir are calculated as follows:

- The length of the weir (L). The selection of the angle α will determine the length of the weir. Its calculation is a function of the discharge coefficient, the hydraulic head, and the design flow.
- The width of the weir wall (t_w) and the internal apex rope (C_c) must both be equal to $P/8$.
- The internal and external apex arc (Arc_{int} , Arc_{ext}) are both functions of t_w and α .

- The length of the cycle wall (l_c), as a function of L , N , Arc_{int} , and Arc_{ext} .
- The length of the platform (B) is a function of L , N , Arc_{int} , Arc_{ext} , α , and t_w .

In this stage, the weir efficiency (ϵ') and the cycle (ϵ'') are also determined, both as a function of L , w , N , and $C_d(\alpha)$. The weir efficiency is also a function of the discharge coefficient of a linear weir; its calculation method is described by Crooskton (2010) [5].

Subsequently, the nappe interference length (B_{int}) is calculated from the ratio H_T/P and the angle α . Finally, the type of aeration of the nappe is determined according to the value of H_T/P and the selected angle α .

(iv) Stage Four: The last stage of the design method includes the dimensionless head relationships for the drowned weir, which were developed and described by Tullis et al. (2007) [38].

The following section describes the results obtained from the studies applied to the discharge flow considered in the proposed sequential design method for the weir; it describes the equations for each variable in detail.

3. Results

3.1. Discharge Coefficient, Weir, and Cycle Efficiency

In this study, the discharge coefficients of circular apex weirs are presented as a function of the ratio H_T/P , whose weir cycle sidewall angles vary from 6° to 20° and are compared with the discharge coefficients reported by Crookston and Tullis (2012) [15] for trapezoidal labyrinth weirs. Both weirs have a half-round crest.

The discharge coefficients $C_d(\alpha)$ of each weir with a circular apex are presented graphically in Figure 8 for $H_T/P \leq 0.8$.

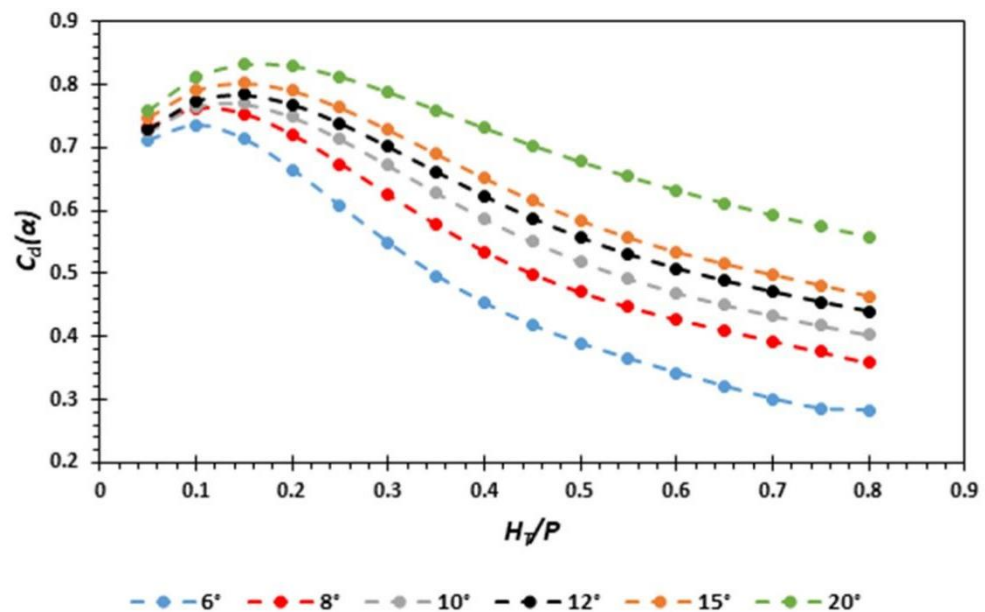


Figure 8. Curves of $C_d(\alpha)$ as a function of H_T/P for different values of α for labyrinth weirs.

The values of the discharge coefficient in Figure 8 were used to obtain a mathematical model of a regressive type through a fifth-degree polynomial equation (Equation (22)) as a function of H_T/P . Weir design methods and curves are mostly generated from empirical equations derived from laboratory experiments [2,5–9]. For example, several researchers reported polynomial equations obtained by non-linear regression to have good fitting [14]. Statistical analysis was used to determine the accuracy of Equation (21) compared to the $C_d(\alpha)$ results obtained from numerical data. The calculated Pearson’s coefficient was very good, varying from 0.999 to 1 for weirs with angles from 6 to 20° . Therefore, Equation (21) provides sufficient accuracy to determine $C_d(\alpha)$. Equations (22)–(27) correspond to the coefficients of Equation (21) as a function of the angle α . The accuracy of predictive Equations (22)–(27) was also evaluated with the numerical results using Pearson’s determination

coefficient, obtaining values of 1 for the case of Equations (22)–(26) and 0.996 for Equation (27). Therefore, reliable results can be obtained using coefficients for Equation (21).

$$C_d(\alpha) = a\left(\frac{H_T}{P}\right)^5 + b\left(\frac{H_T}{P}\right)^4 + c\left(\frac{H_T}{P}\right)^3 + d\left(\frac{H_T}{P}\right)^2 + e\left(\frac{H_T}{P}\right) + f \quad (21)$$

$$a = 42.99 + 48.93\cos(0.1926\alpha) - 24.14\sin(0.1926\alpha) + 7.60\cos(0.3852\alpha) - 15.95\sin(0.3852\alpha) \quad (22)$$

$$b = -61.88 - 65.87\cos(0.2241\alpha) - 4.273\sin(0.2241\alpha) - 22.5\cos(0.4482\alpha) + 5.11\sin(0.4482\alpha) \quad (23)$$

$$c = 47.39 + 36.05\cos(0.2408\alpha) + 14.27\sin(0.2408\alpha) + 13.57\cos(0.4816\alpha) + 3.893\sin(0.4816\alpha) \quad (24)$$

$$d = -20.19 - 11.21\cos(0.2396\alpha) - 4.43\sin(0.2396\alpha) - 4.327\cos(0.4792\alpha) - 1.013\sin(0.4792\alpha) \quad (25)$$

$$e = 3.853 + 2.084\cos(0.2076\alpha) - 0.7578\sin(0.2076\alpha) + 0.5083\cos(0.4152\alpha) - 0.7128\sin(0.4152\alpha) \quad (26)$$

$$f = -5.158 \times 10^{-5}\alpha^4 + 2.591 \times 10^{-3}\alpha^3 - 4.62 \times 10^{-2}\alpha^2 + 0.3487\alpha - 0.3085 \quad (27)$$

The maximum values that can be obtained for the discharge coefficients occur when H_T varies between 0.10 and 0.17 times the height of the weir. Table 6 shows the maximum values of the discharge coefficient for each weir as a function of H_T/P .

Table 6. Maximum values of the discharge coefficient.

α	H_T/P	$C_d(\alpha)$
6°	0.10	0.736
8°	0.11	0.762
10°	0.13	0.771
12°	0.14	0.784
15°	0.15	0.803
20°	0.17	0.833

The discharge coefficients of the circular apex weirs are compared with the trapezoidal apex weirs. The graph in Figure 9 shows the increase in the discharge coefficient of the circular apex weir with respect to the trapezoidal apex, which is 10% when $\alpha = 20^\circ$ to 46% when $\alpha = 6^\circ$, and the slope of the family of curves is significantly higher for $\alpha \leq 10^\circ$.

The weir efficiency (Equation (28)) allows for the hydraulic behavior of a labyrinth weir to be compared with a conventional linear weir, and the advantages obtained by increasing its length can then be determined [23].

$$\epsilon' = \frac{C_d(\alpha)}{C_d(90^\circ)} \frac{L}{W} \quad (28)$$

The cycle efficiency indicator proposed by Willmore (2004) [4] allows for the design of the labyrinth type weir to be optimized and facilitates decision-making. Its calculation is essentially useful for small heads and is obtained from Equation (29).

$$\epsilon'' = C_d(\alpha) \frac{L_{ciclo}}{w} \quad (29)$$

The graphs in Figure 10 represent the efficiency of the labyrinth weir and the cycle as a function of H_T/P . Both graphs show that the maximum efficiency occurs for small values of H_T/P and increases with the decreasing sidewall angle.

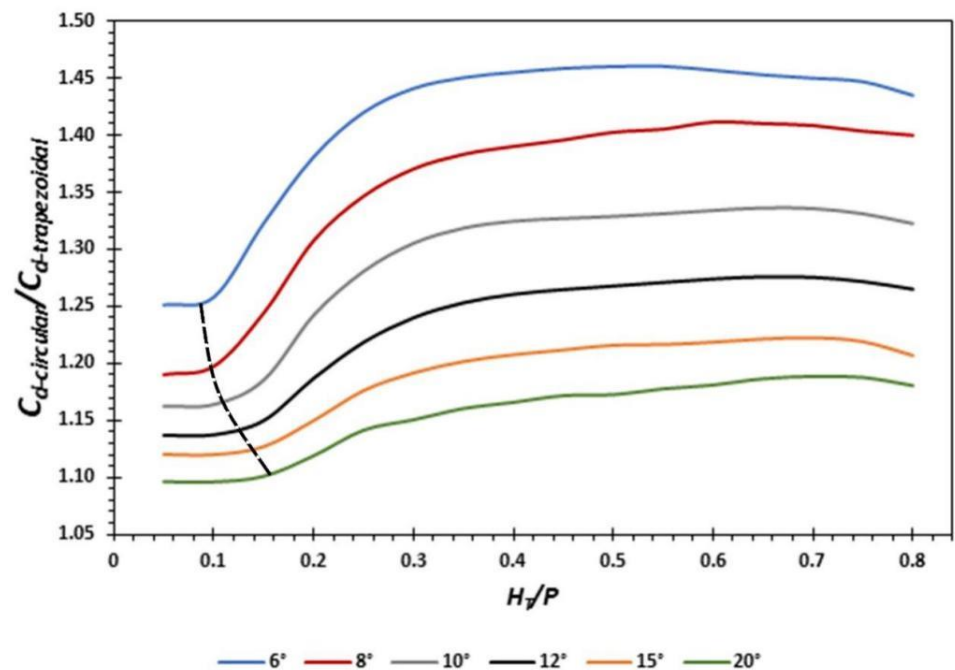


Figure 9. Relationship of the discharge coefficient of the circular apex weir to the trapezoidal apex weir. The dotted line indicates the inflection point on each curve.

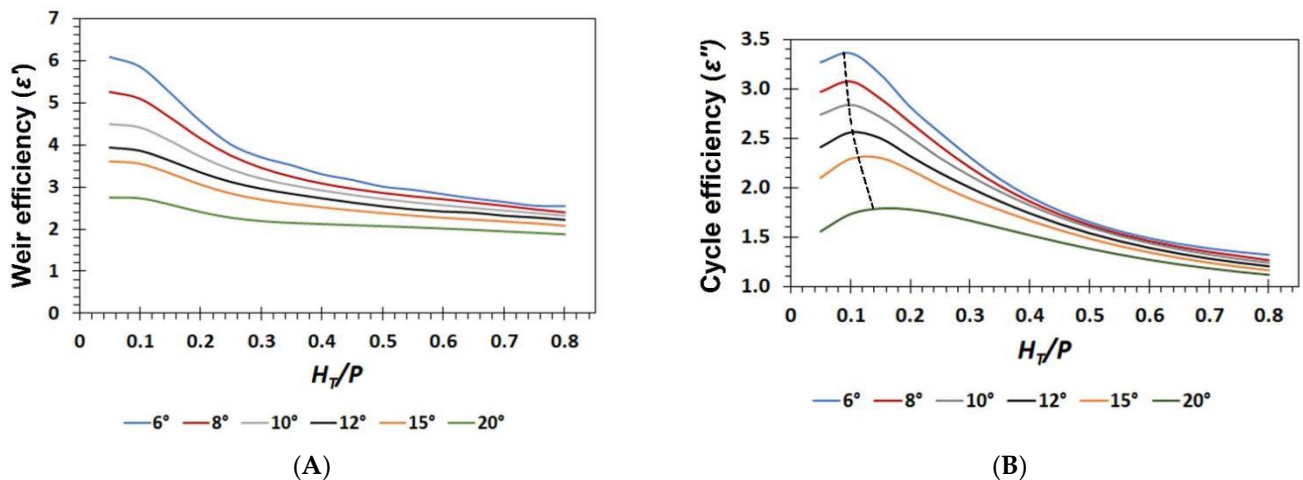


Figure 10. (A) Weir efficiency. (B) Cycle efficiency.

The efficiency of the labyrinth weir, represented by the family of curves in Figure 10A, has an accelerated reduction in its value for $\alpha \leq 10^\circ$ when $H_T/P > 0.1$. Figure 10B represents the cycle efficiency of the weir; the dotted line passes through the values of H_T/P where the maximum efficiency of the cycle is present and coincides with the maximum values of $C_d(\alpha)$.

3.2. Nappe Aeration Conditions

With the increase in the hydraulic head on the weir, four types of aeration were identified (Figure 11): nappe adhered to the wall of the weir, aerated, partially aerated, and drowned.

Table 7 presents the ranges of H_T/P that correspond to the aeration conditions observed for each weir and is included in the family of discharge coefficient design curves (Figure 12).

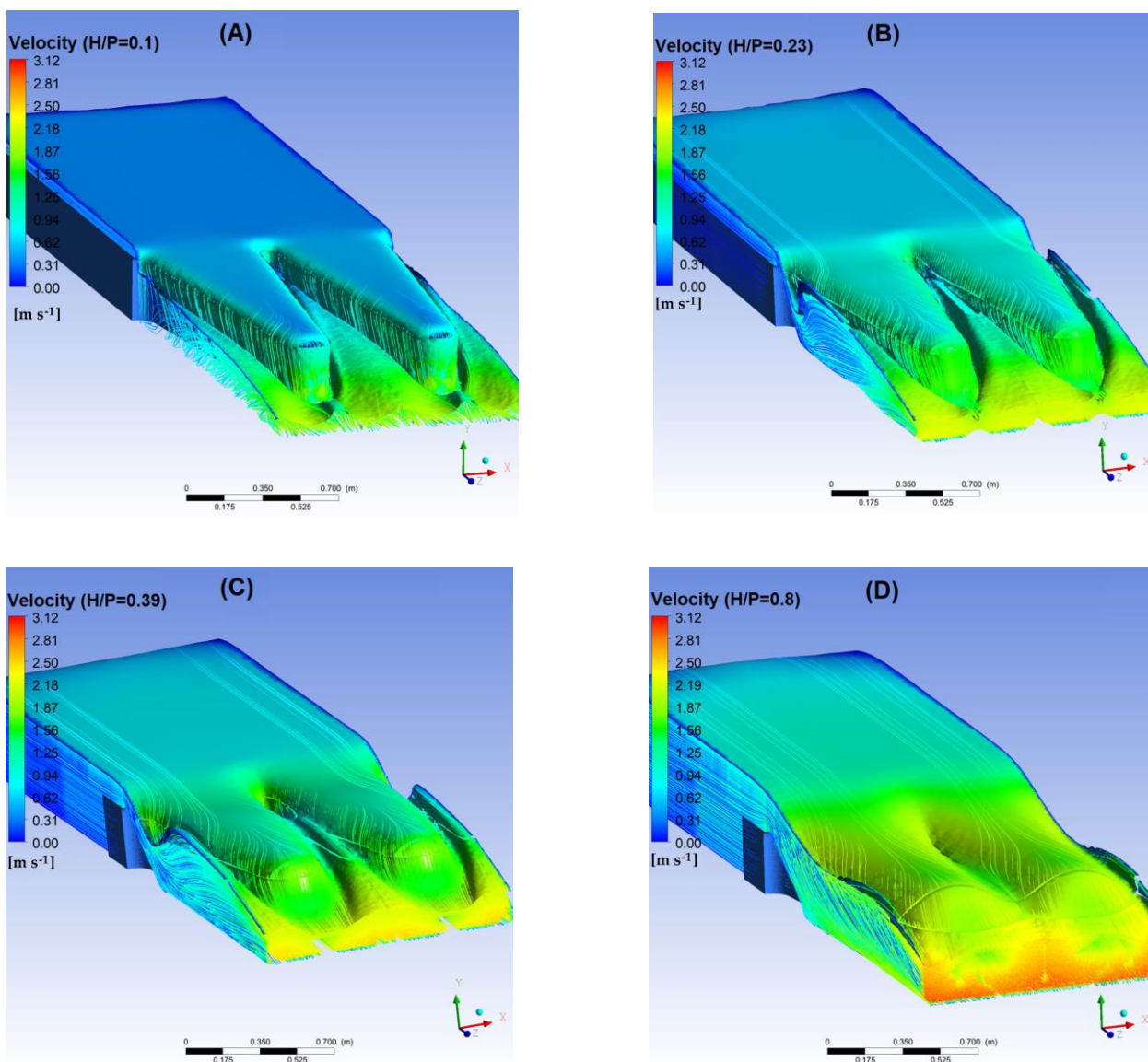


Figure 11. Nappe aeration conditions: (A) clinging, (B) aerated, (C) partially aerated, and (D) drowned.

Table 7. Ranges of nappe aeration conditions.

α (°)	H_T/P			
	Flow Clinging	Flow Aerated	Flow Partially Aerated	Flow Drowned
6°	<0.165	0.165–0.270	0.270–0.487	>0.487
8°	<0.200	0.200–0.350	0.350–0.500	>0.500
10°	<0.265	0.265–0.350	0.350–0.540	>0.540
12°	<0.300	0.300–0.410	0.410–0.550	>0.550
15°	<0.325	0.325–0.400	0.400–0.600	>0.600
20°	<0.450	0.450–0.500	0.500–0.600	>0.600

3.3. Nappe Instability

Nappe instability occurs when the nappe has an oscillating trajectory accompanied by turbulent helical flow adjacent and parallel to the side walls of the weir cycle (Figure 13). Under these conditions, vibration is generated in the weir and may represent a safety hazard for the hydraulic structure.

The results of this work confirm the presence of unstable flow located downstream of the weir, i.e., between the side walls of the weir. The values of H_T/P and the aeration conditions where instability is generated are presented in Table 8 and are included in the discharge coefficient design curves (Figure 14).

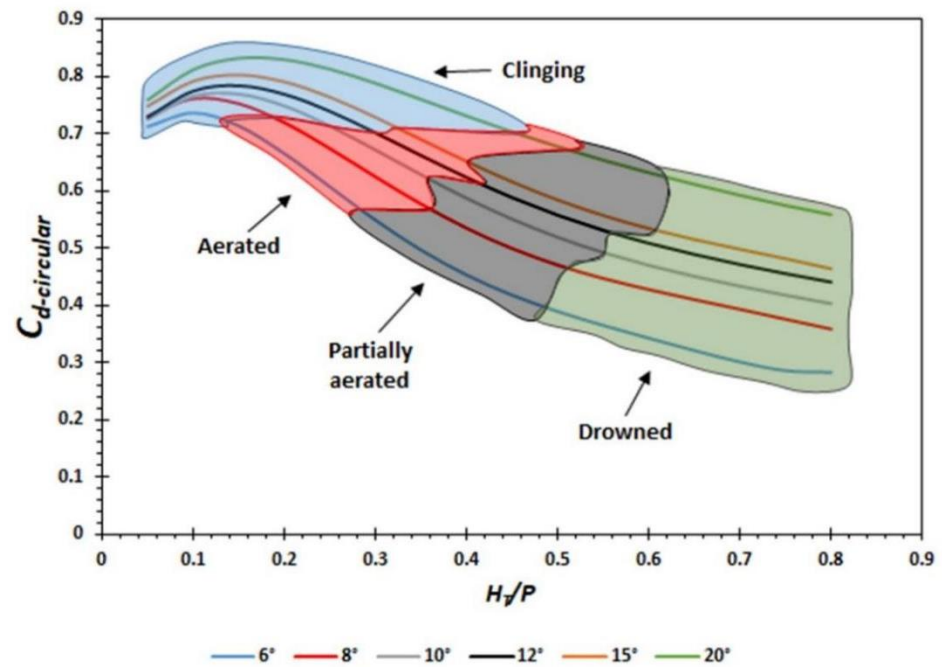


Figure 12. Identification of aeration zones.

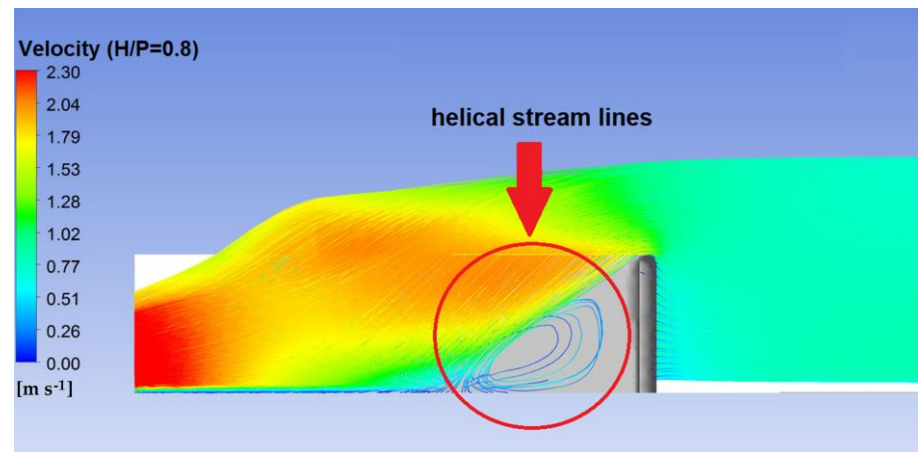


Figure 13. Helical streamlines parallel to the weir wall.

Table 8. Ranges of nappe instability and aeration conditions.

$\alpha(^{\circ})$	Instability	Aeration Condition
6°	-	-
8°	-	-
10°	-	-
12°	$0.56 \leq H_T/P \leq 0.8$	Drowned.
15°	$0.49 \leq H_T/P \leq 0.8$	Partially aerated, and drowned.
20°	$0.40 \leq H_T/P \leq 0.8$	Clinging, aerated, partially aerated, and drowned.

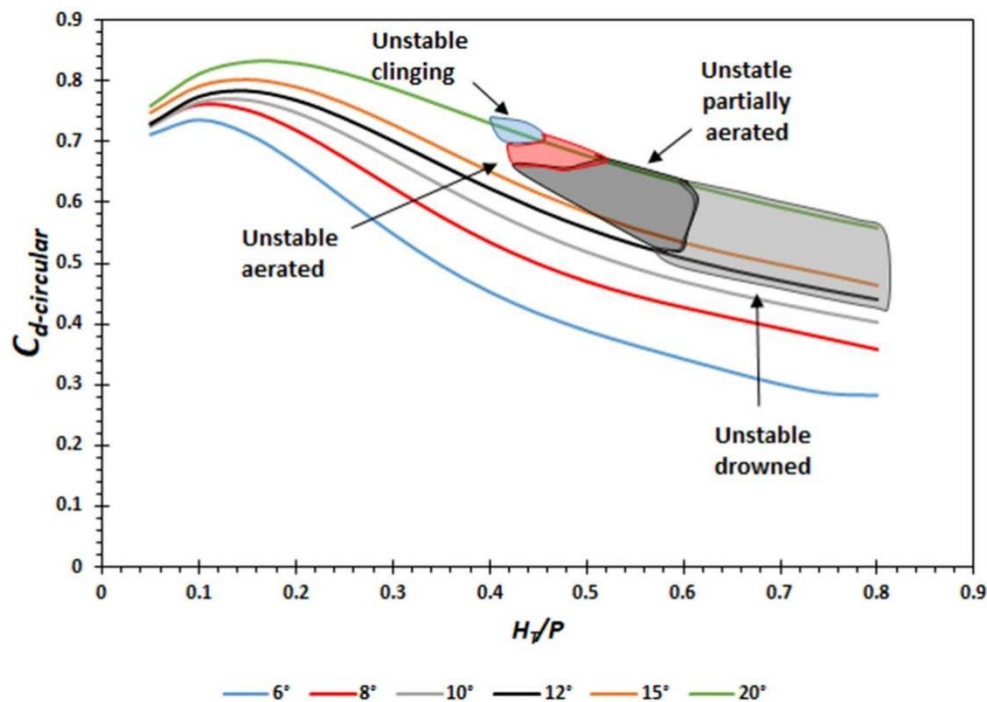


Figure 14. Identification of instability zones.

3.4. Nappe Interference

The effect of the collision between nappes on the reduction of weir efficiency is significant. Therefore, its analysis and behavior are characterized and considered in the design of the weir. The CFD simulations carried out made it possible to visualize the formation of air contrail, accompanied by standing waves or hydraulic jumps between weir cycles (Figure 15A), which decrease with the increasing hydraulic head and presence of drowning in the weir. In weirs where $\alpha \leq 10$, the local drowning at the apexes is generated earlier than in the presence of larger angles (Figure 15B). Furthermore, depending on the aeration condition, turbulent flow may also occur (Figure 16B).

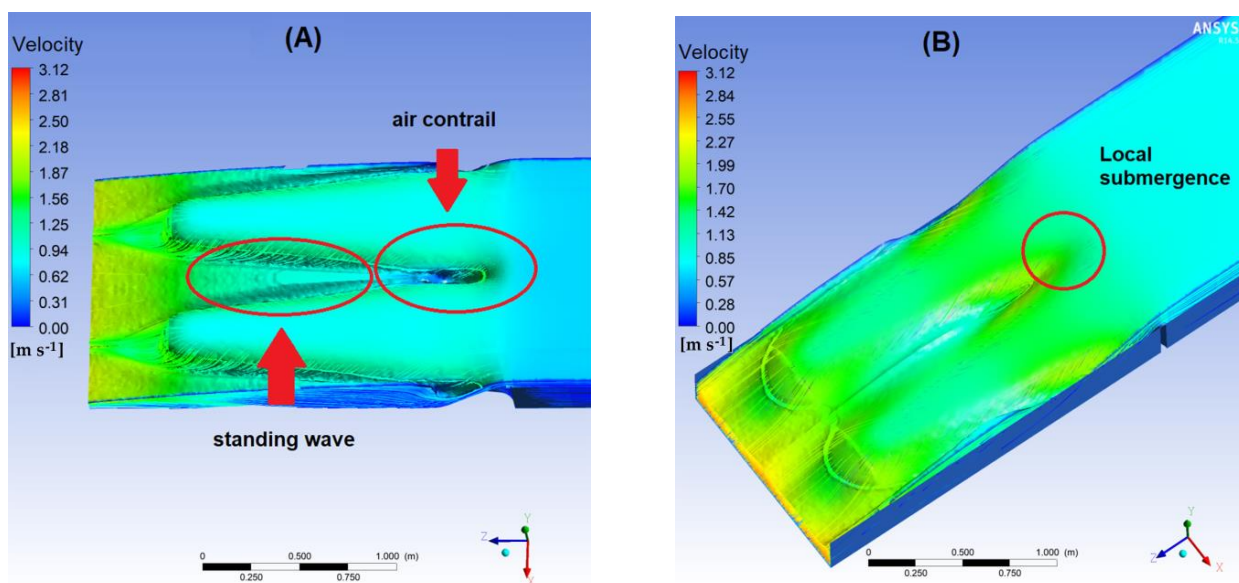


Figure 15. Effects of the nappe interference. (A) Air contrail and standing waves and (B) local drowning.

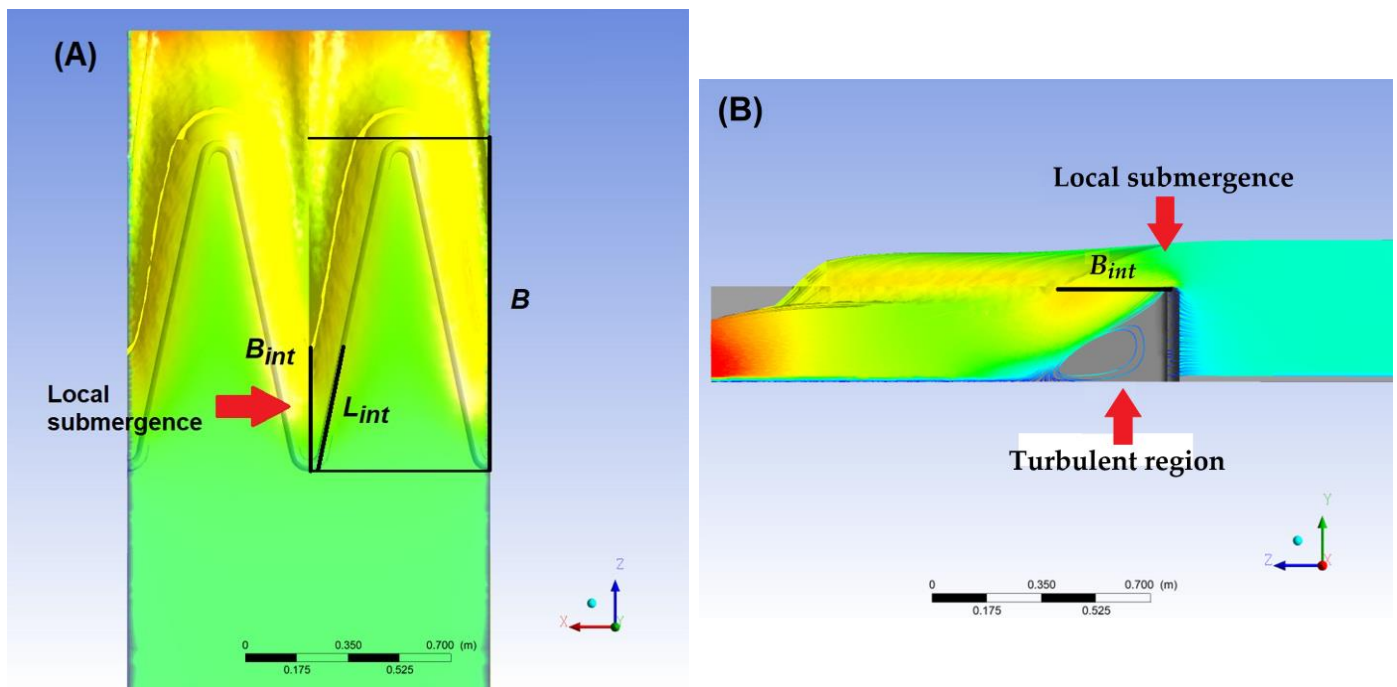


Figure 16. (A) Definition of lengths B_{int} and L_{int} and (B) local drowning and turbulence.

In order to quantify the size of nappe interference, perpendicular measurements (B_{int}) were made from the upstream apex to the point (downstream) where the nappe from the sidewall intersects (Figure 16A). The term L_{int} denotes the projection of B_{int} on the weir crest that is affected by this phenomenon.

The graph in Figure 17 is presented as a family of curves, which are the results of the interference length (B_{int}) in relation to the length of B (perpendicular distance between upstream and downstream apices) for values of $H_T/P \leq 0.8$. The graph allows for the prediction of the length of B_{int} and indicates that its value can vary from 20% to 60% of the length of B in the drowning condition.

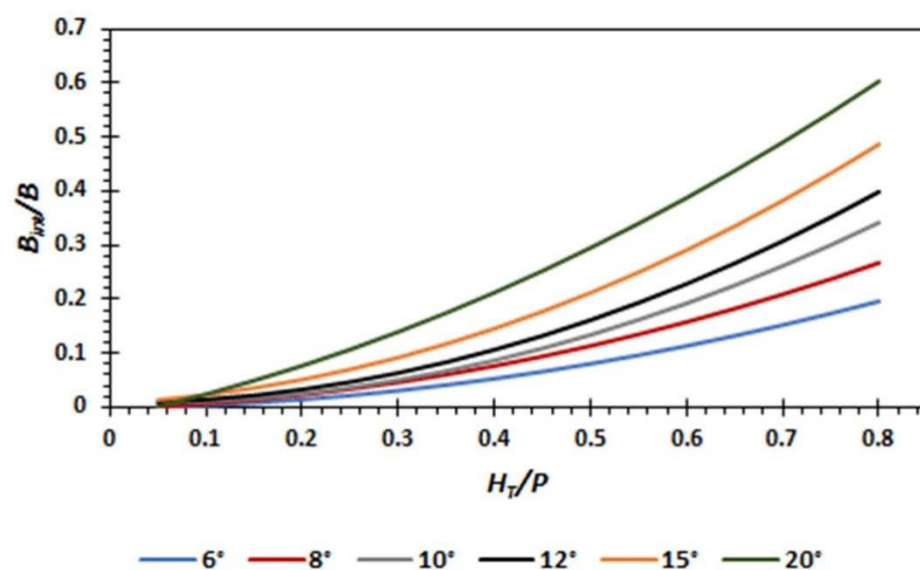


Figure 17. Percentage of the nappe interference in relation to distance B ($6^\circ \leq \alpha \leq 20^\circ$).

To facilitate the use of the graph in Figure 17 in the prediction of the nappe interference length, the family of curves has been modeled through a second-degree equation, as a function of H_T/P (Equation (30)).

$$\frac{B_{int}}{B} = m \left(\frac{H_T}{P} \right)^2 + n \frac{H_T}{P} + o \tag{30}$$

The coefficients of Equation (30) are calculated with Equations (31)–(33) as a function of the angle α .

$$m = 1.284 \times 10^{-4} \alpha^4 - 6.583 \times 10^{-3} \alpha^3 + 0.115 \alpha^2 - 0.764 \alpha + 1.978 \tag{31}$$

$$n = -1.095 \times 10^{-4} \alpha^4 + 5.648 \times 10^{-3} \alpha^3 - 0.01 \alpha^2 + 0.722 \alpha - 1.781 \tag{32}$$

$$o = 6.004 \times 10^{-6} \alpha^4 - 3.349 \times 10^{-4} \alpha^3 + 0.006 \alpha^2 - 0.046 \alpha + 0.110 \tag{33}$$

3.5. Application of the Proposed Method

As a case study, information from Houston (1982) [9] on the Ute Dam weir in Logan, New Mexico was studied.

The design procedure followed the method proposed by Hay and Taylor (1979) [11], i.e., the original design was for a 10-cycle weir based on the design curves of Hay and Taylor (1970) [11]. However, it did not pass the desired design discharge within the maximum elevation of the reservoir. A 14-cycle weir, designed according to the criteria of the laboratory channel tests conducted by the Bureau of Reclamation, satisfactorily met the required discharge and water surface elevation [9]. To avoid instability and oscillations of the nappe and provide aeration, two dividers were placed at the crest of each cycle, 3.35 m upstream from the downstream apex of the cycle. The weir design was based on a family of dimensionless ratio curves L/W , in the graph Q/Q_N versus H_T/P , where Q/Q_N is the discharge magnification and Q_N is the discharge over a linear weir. The results reported by Houston (1982) [9] on the weir design are summarized in Table 9 and Figure 18.

Table 9. Dimensions of the labyrinth weir of the Ute Dam [8].

Concept	Symbol	Value-Unit	Observations
(i) Initial data			
Design flow	Q	15,574 m ³ /s	Initially, the design discharge was 16,042 m ³ /s.
Weir width	W	256 m	-
Weir height	P	9.14 m	-
Upstream total head	H_T	5.79 m	-
(ii) Geometric variables and non-dimensional relationships			
Head water ratio	H_T/P	0.63	$0.05 \leq H_T/P \leq 1$ (upper range is expanded from 0.5 to 1 to use the design curves)
Flow magnification	Q/Q_N	2.4	-
Angle of sidewall	α	12.1475°	-
Length magnification	L/W	4	$2 \leq L/W \leq 8$.
Vertical aspect ratio	w/P	2	$2 \leq w/P \leq 5$
Cycle width	w	18.29 m	-
Number of cycles	N	14	-
Weir length	L	1024.24 m	-
Sidewall length	l_c	34.76 m	-
Length between apexes	B	33.99 m	-
Apex	A	1.82 m	-
Crest radius	R_{Crest}	0.30	-
Upper crest width	t_{w-1}	0.61 m	-
Lower crest width	t_{w-2}	1.52 m	-

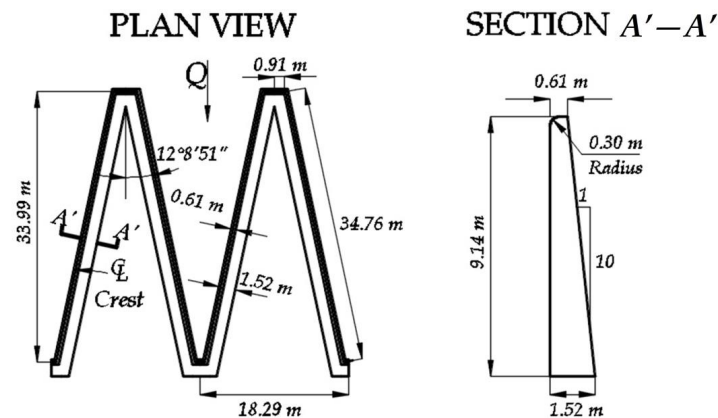


Figure 18. Shape and dimensions of the 14-cycle labyrinth weir [9].

The design sequence shown in Table 10 and in the flowchart in Figure 19 was used as an example of the application of the proposed design methodology for the Ute Dam weir.

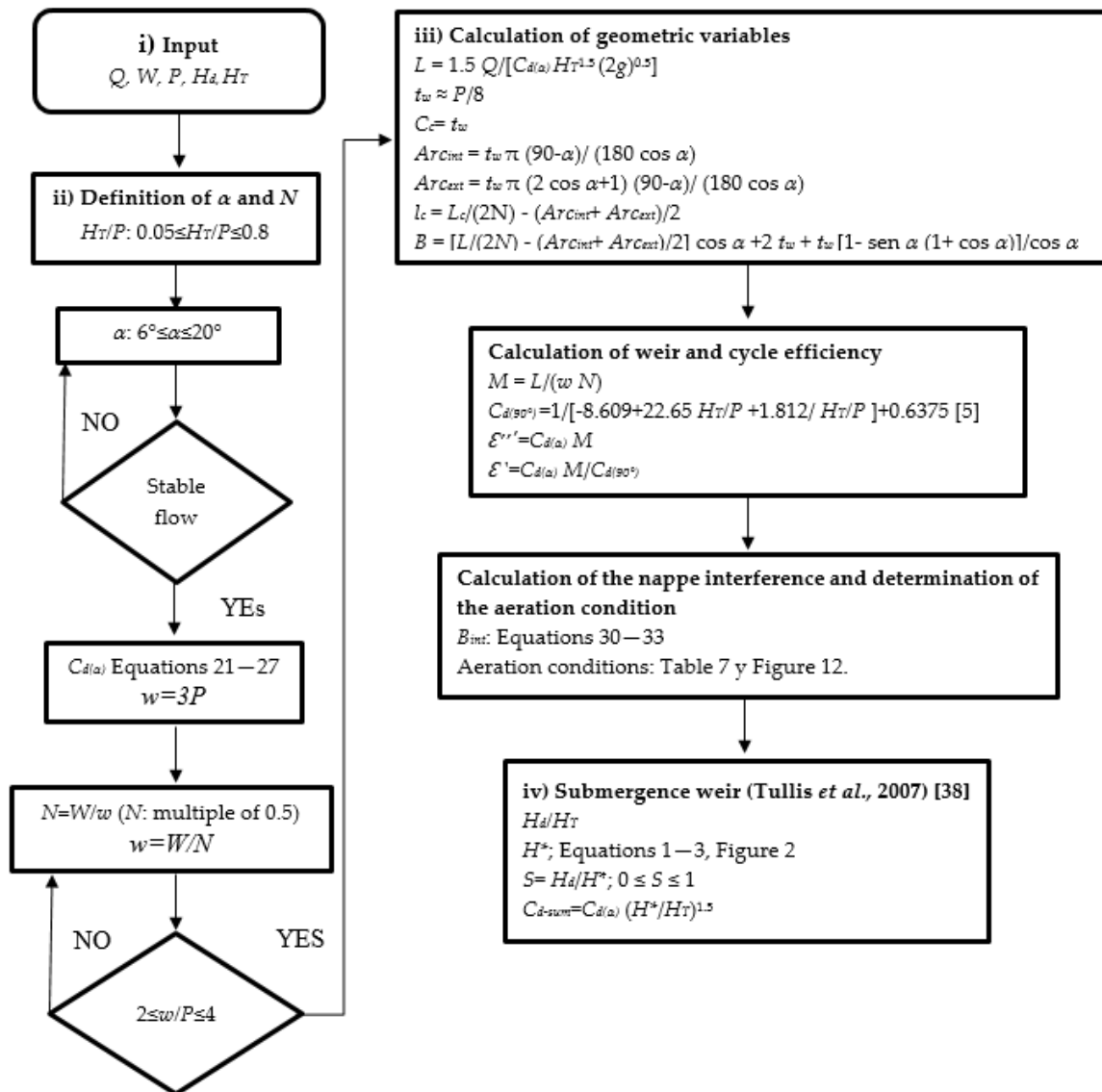


Figure 19. Flowchart for the design procedure.

Table 10. Spreadsheet for the design of the labyrinth weir.

Concept	Symbol	Value-Unit	Equations and Limits
(i) Input data			
Design flow	Q	15,574 m ³ /s	-
Weir width	W	256 m	-
Weir height	P	9.14 m	-
Upstream total head	H_T	5.79 m	-
(ii) Definition of α and the number of cycles (N)			
Head water ratio	H_T/P	0.63	$0.05 \leq H_T/P \leq 0.8$
Angle of sidewall	α	11.5°	$6^\circ \leq \alpha \leq 20^\circ$
Nappe stability	-	Stable	Stable/Unstable: Table 8 and Figure 14
Labyrinth weir discharge coefficient	$C_d(\alpha)$	0.483	$C_d(\alpha) = f(H_T/P, \alpha)$, Equations (21)–(27)
Cycle width	w	27.42 m	$w = 3P$
Number of cycles	N	9	$N = W/w$
New cycle width	w	28.44 m	$w = W/N$
Vertical aspect ratio	w/P	3.11	$2 \leq w/P \leq 4$
(iii) Calculation of geometric variables, weir and cycle efficiencies, nappe interference and aeration condition			
Geometric variables			
Total centerline length of weir	L	783.20 m	$L = 1.5Q / [C_d(\alpha)HT^{1.5}(2g)^{0.5}]$
Wall width	t_w	1.14 m	$t_w \approx P/8$
Internal apex rope	C_c	1.14 m	$C_c = t_w$
Internal apex arc	Arc_{int}	1.60 m	$Arc_{int} = t_w \pi (90 - \alpha) / (180 \cos \alpha)$
External apex arc	Arc_{ext}	1.16 m	$Arc_{ext} = t_w \pi (2 \cos \alpha + 1) (90 - \alpha) / (180 \cos \alpha)$
Centerline length of sidewall	l_c	42.14 m	$l_c = L / (2N) - (Arc_{int} + Arc_{ext}) / 2$
Length of apron	B	44.28 m	$B = [L / (2N) - (Arc_{int} + Arc_{ext}) / 2] \cos \alpha + 2t_w + t_w [1 - \sin \alpha (1 + \cos \alpha)] / \cos \alpha$ (or input data)
Weir and cycle efficiency			
Magnification ratio	M	3.17	$M = L / (wN)$
Linear weir coefficient discharge	$C_d(90^\circ)$	0.754	$C_d(90^\circ) = 1 / [-8.609 + 22.65HT/P + 1.812/HT/P] + 0.6375$ [5]
Cycle efficiency	ϵ''	0.74	$\epsilon'' = C_d(\alpha)M$
Weir efficiency	ϵ'	1.96	$\epsilon' = C_d(\alpha)M / C_d(90^\circ)$
Nappe interference length and aeration condition			
Nappe interference length	B_{int}	10.89 m	Equations (30)–(33)
Aeration condition	-	Drowned	Table 7 and Figure 12
(iv) Submergence (Tullis et al., 2007 [38])			
Downstream total head	H_d	1.22 m	-
Head ratio	H_d/H_T	0.21	-
Submergence upstream total head	H^*	5.84 m	Equations (1)–(3) and Figure 2
Submergence level	S	0.20	$S = H_d/H^*$; $0 \leq S \leq 1$
Submerged weir discharge coefficient	C_{d-sum}	0.476	$C_{d-sum} = C_d(\alpha)(H^*/HT)^{1.5}$

4. Discussion

4.1. Discussion of Discharge Coefficient, Weir, and Cycle Efficiency

The magnitude of the discharge coefficient C_d helps us to understand the hydraulic behavior of a weir and is essential when making decisions during weir design, where its value depends on geometry, aeration conditions, and flow behavior during the discharge. When the ratio $H_T/P < 0.2$, higher values of $C_d(\alpha)$ up to 0.833 are presented; this is when the nappe is adhered to the weir wall. During the transition of a nappe adhered to the wall becoming partially aerated, there is an accelerated decrease in $C_d(\alpha)$ values at weirs with angles varying from 6° to 10°. The reduction is less abrupt when $\alpha \geq 12^\circ$ and, as the head H_T on the weir increases, the value of $C_d(\alpha)$ decreases. For values of $H_T/P < 0.1$, the 8° and 10° weirs exhibit similar behavior in $C_d(\alpha)$, and the $C_d(\alpha)$ of the 12° weir is slightly higher than that of the 10° weir. The higher angle weirs have better discharge capacities. However, lower angle weirs have the advantage of having a longer weir crest length.

The increase of the discharge coefficient of the circular apex weir, with respect to the trapezoidal apex weir, is immediate from $H_T/P \geq 0.1$. In addition, the dotted line in Figure 9 indicates the inflection point of each curve, where the discharge coefficients acquire their maximum value (Table 6). In effect, the slopes increase until the nappe is no

longer aerated and presents local drowning at the weir apex. When the weirs work in a drowned manner, efficiency decreases, projecting curves with slightly descending slopes at the end.

The weir and cycle efficiency values decrease when the nappe is no longer adhered to the wall and occurs earlier in weirs where $\alpha \leq 10$. In addition, when the weir begins to drown, the efficiencies generate minimum values, stabilizing from $H_T/P > 0.8$.

In Figure 10A, the immediate reduction in weir efficiency occurs when local drowning at the apex upstream of the weir becomes present. On the other hand, in Figure 10B, it has been observed that the reduction of the cycle efficiency for $\alpha \leq 10^\circ$ is almost immediate after presenting its maximum value; this phenomenon is due not only to the presence of local drowning, but also to the change of aeration regime of the nappe.

4.2. Discussion of Nappe Aeration Conditions

According to the values of the discharge coefficient, it has been identified that the weir is more efficient when the nappe is adhered to the wall. In fact, when the flow is aerated, the discharge coefficient decreases and sub-atmospheric pressures occur behind the nappe. When the flow is in a transitional or partially aerated state, the air cavities under the nappe are removed. Finally, when the weir begins to be drowned, it is characterized by presenting a thicker nappe without the presence of air cavities. The weir is also at its minimum efficiency, remaining constant from $H_T/P > 0.8$. In the latter case, the behavior of the weir is equivalent to that of the linear weir.

Depending on the aeration condition, turbulent flow has been observed on the walls of the channel. For 20° weirs, aeration conditions tend to occur under turbulent flow when the nappe is adhered to the weir wall, while partially aerated conditions occur for 15° to 20° weirs, and drowned conditions for 12° to 20° weirs, as shown on Table 9. Turbulent flow can also occur between the walls of the cycle as the weir head increases, with greater occurrence under drowned conditions and lesser occurrence when the nappe is adhered to the weir wall.

All the weirs have the nappe adhered to the wall when $H_T/P \leq 0.16$. On the other hand, it has been observed that, with an increase of the angle α , the presence of this regime increases up to $H_T/P \approx 0.45$. However, when $\alpha = 20^\circ$, the opposite occurs for the case of the aerated regime, i.e., its presence is lower when the angle α increases. The value of the discharge coefficient presents a rapid decrease for angles that vary from 6° to 10° , and this is when the transition from clinging flow to aerated flow occurs. When $15^\circ \leq \alpha \leq 20^\circ$, the weir has a greater range of flow clinging to the wall, in contrast to the aerated flow condition that is briefly produced by changing to the partially aerated regime. The drowning condition is generated for larger heads, i.e., when $H_T/P > 0.49$ ($\alpha = 6^\circ$).

4.3. Discussion of Nappe Instability and Interference

From $\alpha \geq 12^\circ$, the presence of turbulent flow and helical streamlines was detected on the wall cycles and accompanied by changes in the aeration condition. According to the simulations carried out, the instability is more prevalent when the nappe is partially aerated or drowned than when it is clinging or aerated.

On the other hand, the effect of collision between nappes on the reducing of weir efficiency was demonstrated and, therefore, its behavior was characterized for the labyrinth weir design. The length of the nappe interference is a function of the hydraulic load and the sidewall angle of the cycles. Figure 20 shows that weirs with $\alpha \geq 12^\circ$ tend towards a stable value of crest length affected by the nappe interference, for similar values of H_T/P . On the other hand, it should be noted that weirs where $\alpha < 10^\circ$ have a shorter crest length affected by the nappe interference.

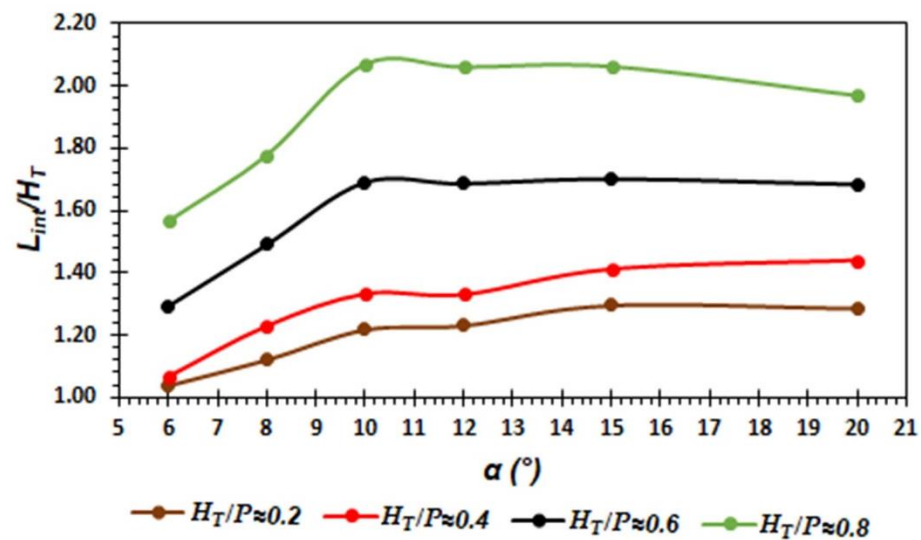


Figure 20. Length of the crest affected by the nappe interference.

4.4. Discussion of Application of the Proposed Method

The geometric differences of the weir and the crest presented in the Houston (1982) [9] report and the one analyzed in this work are evident. The shape of the crest influences the behavior of the nappe as aeration, in the nappe interference, and, most importantly, flow instability in the discharge. The weir crest of the Ute Dam has a quarter-rounded shape. However, a half-round shape, as recommended in the proposed design, helps the flow to remain adhered to the weir wall, which increases its efficiency; if the flow separates then efficiency is lost [5,42]. The design of the Ute Dam weir followed the procedure of Hay and Taylor (1970) [11]. This means that it considered the w/P ratio to be equal to 2, which resulted in a weir of 14 cycles, and a total length of 1024.24 m was obtained. The latter was determined from the flow magnification and the dimensionless L/W ratio, with a sidewall angle of 12.15° to design the discharge required for a certain reservoir level. The triangular shape of the downstream wall of the weir caused a greater length of nappe interference to be produced, which translated into a lower discharge capacity. The design method proposed here considered that the w/P ratio ≈ 3 , assuming a conservative value between the limits of w/P reported by Hay and Taylor (1972) [11] and Tullis et al. (1995) [14], for the weir to be efficient. The number of cycles was reduced to nine, and the total length of the weir was reduced to 783.20 m, as determined by the general discharge equation for weirs, thus discharging the required design discharge. However, the length of platform B was increased from 10.29 m to 44.28 m, and a maximum sidewall angle of 11.5° was chosen to avoid generating flow instability.

The Bureau of Reclamation spillway design [9] has two dividers in each cycle to reduce the instability and oscillations of the nappe. However, this method is not recommended [26] due to the number of dividers required, incurring the possible danger of failure of the hydraulic structure. The proposed sequential design method indicates the ranges of H_T/P and the aeration conditions in which the instability originates, which is an important indicator at the time of design.

The sequential design method proposed in the present work is a complete method because it considers the flow behavior during discharge and the possible instability of the nappe. They are integrated in the design table in Table 10 and in the flowchart in Figure 19. However, it is limited for values of H_T/P (from 0.5 to 0.8), sidewall angles from 6° to 20° , and for weirs located in a channel.

In the design of a labyrinth weir, it is undoubtedly advisable to perform physical modeling, together with numerical modeling, to validate the hydraulic performance of the labyrinth weir. The design method, design graphs, and charts are limited to the geometries and hydraulic conditions analyzed in this study.

5. Conclusions

The design procedure of a circular apex labyrinth weir is presented based on its geometric characteristics and the discharge flow behavior. To generate design parameters, the experimental results of the discharge coefficient reported in the literature, were first validated, and verified in CDF and later incorporated into the proposed design method for labyrinth weirs.

The proposed design procedure applies to weirs where $H_T/P \leq 0.8$ and $6^\circ \leq \alpha \leq 20^\circ$. The values of the discharge coefficient are presented as a family of curves as function of H_T/P and using a mathematical model of a regressive type (through a fifth-degree polynomial equation found for this purpose). The results indicate a higher discharge capacity of the weir while increasing the angle α . The contrast between the discharge coefficients of circular apex weirs with those of a trapezoidal apex indicate an increase in their value of up to 46% ($\alpha = 6^\circ$) in relation to the trapezoidal apex weir. The cycle and weir efficiency are presented as a tool in the design procedure. Both parameters indicate that the maximum values occur for $H_T/P \leq 0.17$ and the efficiencies are higher with the reduction of the angle α .

Four aeration conditions were identified (clinging, aerated, partially aerated, and drowned) with ranges of H_T/P for each condition. The relationship between the discharge coefficient and the aeration condition is evident: when the nappe is adhered to the wall, the weir has a higher discharge coefficient value. In addition, its presence is greater when α increases, and the opposite occurs when the nappe is aerated.

Nappe instability occurs when $12^\circ \leq \alpha \leq 20^\circ$ and it is accompanied by changes in aeration conditions; there is a greater presence when the flow is partially aerated and drowned. Similarly, ranges of H_T/P were identified when instability occurred. It is necessary not to incur the instability ranges when designing the weir to avoid possible damage to the hydraulic structure.

The length of the crest affected by the nappe interference was characterized and quantified. For this purpose, a family of curves B_{int}/B is presented herein as a function of H_T/P , and a mathematical model was found for its estimation. This model is a second-degree equation. The results show that the length of B_{int} reaches a maximum of 60% of the length of B .

A flowchart implemented in a spreadsheet is also presented as a tool to guide the design process of a labyrinth weir, considering its geometric variables and the phenomena that occur in the discharge flow. Additionally, the drowning study carried out by Tullis et al. (2007) [38] is also considered.

The proposed sequential method for the design of a labyrinth weir represents a contribution to the improvement of the hydraulic performance of weirs of this type of hydraulic structure. It should be noted that this proposal takes into consideration parameters such as the following: (a) flow stability during discharge, (b) aeration condition of the nappe, (c) the nappe interference length, (d) weir and cycle efficiencies, and (e) weir drowning [38], which have been traditionally ignored in traditional design methods or have been studied independently [1,6,10–12]. In addition, Tullis et al. (1995) [14] and Crookston and Tullis (2012) [15] generated spreadsheets to help in the weir design. However, they did not include the nappe aeration and its instability conditions, as well as the length of the nappe interference, which influences the efficiency of the weir operation and the safety of the hydraulic structure. Finally, although the methods and tools presented in this study were highly effective when used in the design and study of a labyrinth weir, it is recommended that physical and numerical modeling be performed to validate the hydraulic performance of a specific pre-designed hydraulic structure with the proposed sequential method.

Author Contributions: Conceptualization, W.O.-B. and C.D.-D.; methodology, E.D.M.-V. and W.O.-B.; software, E.D.M.-V. and J.F.-V.; validation, E.D.M.-V., H.S.-T. and W.O.-B.; formal analysis, C.D.-D. and H.S.-T.; investigation, E.D.M.-V.; resources, C.B.C.; writing—original draft preparation, E.D.M.-V. and W.O.-B.; writing—review and editing, H.S.-T., C.D.-D. and C.B.C.; visualization, E.D.M.-V. and

J.F.-V.; supervision, W.O.-B.; project administration, W.O.-B.; funding acquisition, W.O.-B. and C.B.C. All authors have read and agreed to the published version of the manuscript.

Funding: This research received no external funding.

Data Availability Statement: Not applicable.

Conflicts of Interest: The authors declare no conflict of interest.

Abbreviations

A	internal length apex.
Arc_{int}	internal apex arc.
Arc_{ext}	external apex arc.
A_x, A_y, A_z	fractional area in the x, y, z direction, respectively.
a	adjustment factor to obtain the discharge coefficient.
B	length of apron.
B_{int}	nappe interference length.
b	adjustment factor to obtain the discharge coefficient.
c	adjustment factor to obtain the discharge coefficient.
C_d	discharge coefficient.
C_{d-sum}	submerged weir discharge coefficient.
$C_d(\alpha)$	labyrinth weir discharge coefficient
$C_d(90^\circ)$	linear weir discharge coefficient.
C_c	internal apex rope.
$C_{1\epsilon}, C_{2\epsilon}, C_\mu$	constants of the turbulent k- ϵ model.
Cov	covariance.
D	external apex length.
Dk_{eff}	effective diffusivity for turbulent kinetic energy.
$D\epsilon_{eff}$	effective diffusivity for dissipation rate.
d	adjustment factor to obtain the discharge coefficient.
e	adjustment factor to obtain the discharge coefficient.
F_D	diffusion term.
F_S	source term.
F_s	security factor.
f	adjustment factor to obtain the discharge coefficient.
f_i	control variable.
f_x, f_y, f_z	viscous acceleration in x, y, z direction, respectively.
G_k	turbulent kinetic energy generation due to mean velocity gradients.
G_x, G_y, G_z	acceleration of the body in the x, y, z direction, respectively.
g	acceleration gravity.
H_d	downstream total head.
H_T	upstream total head.
H^*	upstream total head of the drowned weir.
h	piezometric head.
k	turbulent kinetic energy.
L	characteristic length of the weir.
L_{cycle}	cycle length.
L_{int}	length of the crest affected by the nappe interference.
l_C	centerline length of sidewall.
M	magnification ratio.
m	adjustment coefficient to obtain the length B_{int} .
N	number of cycles.
N_C	number of cells.
n	adjustment coefficient to obtain the length B_{int} .
o	adjustment coefficient to obtain the length B_{int} .
P	weir height.
p	order of convergence.
Q	design flow.

Q_N	flow of a linear weir.
R_{crest}	radius of the weir crest.
r	mesh refinement ratio.
S	submergence level.
S_{ij}^2	strain rate tensor.
t_w	weir wall width.
t_{w-1}	upper crest width.
t_{w-2}	lower crest width.
u	velocity component in the x direction.
V_F	fraction volume.
v	velocity component in y direction.
ν_t	turbulent kinematic viscosity.
W	channel width.
w	cycle width.
Y_{exp}	experimental results.
Y_{num}	numerical results.
z	velocity component in z direction.
α	angle of sidewall.
ΔV_i	volume of the i-th cell.
γ	representative cell size.
ϵ	dissipation rate.
ϵ	relative error.
ϵ'	weir efficiency.
ϵ''	cycle efficiency.
σ_{exp}^2	variance of the experimental results.
σ_{num}^2	variance of the numerical results.
σ_ϵ	Prandtl number.

References

- Mattos-Villarreal, E.D.; Flores-Velazquez, J.; Ojeda-Bustamante, W.; Iniguez-Covarrubias, M.; Diaz-Delgado, C.; Salinas-Tapia, H. Hydraulic analysis of a compound weir (triangular-rectangular) simulated with computational fluid dynamics (CFD). *Technol. Cienc. Agua* **2021**, *12*, 112–162. [[CrossRef](#)]
- Darvas, L.A. Discussion of performance and design of labyrinth weirs, by Hay and Taylor. *J. Hydraul. Eng. ASCE* **1971**, *97*, 1246–1251. [[CrossRef](#)]
- Bilhan, O.; Emiroglu, E.; Miller, C.J. Experimental investigation of discharge capacity of labyrinth weirs with and without nappe breakers. *World J. Mech.* **2016**, *6*, 207–221. [[CrossRef](#)]
- Willmore, C. Hydraulic Characteristics of Labyrinth Weirs. Master's Thesis, Utah State University, Logan, Utah, April 2004.
- Crookston, B. Labyrinth Weirs. Ph.D. Thesis, Utah State University, Logan, Utah, December 2010.
- Tullis, B.; Young, J. *Lake Brazos Dam Model Study of the Existing Spillway Structure and a New Labyrinth Weir Spillway Structure*; Report No. 1575; Utah Water Research Laboratory: Logan, Utah, 2005.
- Magalhães, A.; Lorena, M. *Hydraulic Design of Labyrinth Weirs*; Report No. 736; National Laboratory of Civil Engineering: Lisboa, Portugal, 1989.
- Houston, K. *Hydraulic Model Study of Hyrum Dam Auxiliary Labyrinth Spillway*; Report No. GR-82-13; U.S. Bureau of Reclamation: Denver, Colorado, 1983.
- Houston, K. *Hydraulic Model Study of Ute Dam Labyrinth Spillway*; Report No. GR-82-7; U.S. Bureau of Reclamation: Denver, Colorado, 1982.
- Tullis, B.; Crookston, B.M. *Lake Townsend Dam Spillway Hydraulic Model Study Report*; Utah Water Research Laboratory: Logan, Utah, 2008.
- Hay, N.; Taylor, G. Performance and design of labyrinth weirs. *J. Hydraul. Div.* **1970**, *96*, 2337–2357. [[CrossRef](#)]
- Hinchliff, D.; Houston, K. *Hydraulic Design and Application of Labyrinth Spillways*; Division of Research Engineering and Research Center, Bureau of Reclamation: Denver, Colorado, 1984.
- Lux, F., III. Design and application of labyrinth weirs. In *Design of Hydraulic Structures 89*; Alberson, M.L., Kia, R.A., Eds.; Balkema/Rotterdam/Brookfield: Toronto, ON, Canada, 1989; pp. 205–215.
- Tullis, J.P.; Amanian, N.; Waldron, D. Design of labyrinth spillways. *J. Hydraul. Eng.* **1995**, *121*, 247–255. [[CrossRef](#)]
- Crookston, B.M.; Tullis, B.P. Hydraulic design and analysis of labyrinth weirs. I: Discharge relationships. *J. Irrig. Drain. Eng.* **2012**, *139*, 363–370. [[CrossRef](#)]
- Idrees, A.K.; Al-Ameri, R. A review of hydraulic performance and design methods of labyrinth weirs. *Water Suppl.* **2022**, *22*, 8120–8138. [[CrossRef](#)]

17. Savage, B.; Frizell, K.; Crowder, J. Brains versus brawn: The changing world of hydraulic model studies. In Proceedings of the Annual Conference Association of State Dam Safety Officials (ASDSO), Phoenix, AZ, USA, 26–30 September 2004.
18. Paxson, G.; Savage, B. Labyrinth spillways: Comparison of two popular USA design methods and consideration of non-standard approach conditions and geometries. In *International Junior Researcher and Engineer Workshop on Hydraulic Structures*; Report CH61/06; The University of Queensland: Brisbane, Australia, 2006.
19. Chanel, P.G.; Doering, J.C. Assessment of spillway modeling using computational fluid dynamics. *Can. J. Civ. Eng.* **2008**, *35*, 1481–1485. [[CrossRef](#)]
20. Aydin, M.C.; Emiroglu, M.E. Determination of capacity of labyrinth side weir by CFD. *Flow Meas. Instrum.* **2013**, *29*, 1–8. [[CrossRef](#)]
21. Savage, B.M.; Crookston, B.M.; Paxson, G.S. Physical and numerical modeling of large headwater ratios for a 15 labyrinth spillway. *J. Hydraul. Eng.* **2016**, *142*, 04016046. [[CrossRef](#)]
22. Crookston, B.M.; Anderson, R.M.; Tullis, B.P. Free-flow discharge estimation method for Piano Key weir geometries. *J. Hydro-Environ. Res.* **2018**, *19*, 160–167. [[CrossRef](#)]
23. Ben Said, M.; Hafnaoui, M.A.; Madi, M. Numerical analysis of the influence of approach flow conditions on the efficiency of labyrinth weir. *Model. Earth Syst. Environ.* **2022**, 1–11. [[CrossRef](#)]
24. Samadi, A.; Salmasi, F.; Arvanaghi, H.; Mousaviraad, M. Effects of Geometrical Parameters on Labyrinth Weir Hydraulics. *J. Irrig. Drain. Eng.* **2022**, *148*, 06022006. [[CrossRef](#)]
25. Lux, F., III; Hinchliff, D. Design and construction of labyrinth spillways. In Proceedings of the 15th International Congress on Large Dams, International Commission on Large Dams, Paris, France, 15–19 November 1985.
26. Crookston, B.M.; Tullis, B.P. Labyrinth weirs: Nappe interference and local submergence. *J. Irrig. Drain. Eng.* **2012**, *138*, 757–765. [[CrossRef](#)]
27. Falvey, H.T. *Hydraulic Design of Labyrinth Weirs*; American Society of Civil Engineers (ASCE): Reston, VA, USA, 2003; pp. 31–108. [[CrossRef](#)]
28. Hauser, G. *Design of Aerating Weirs*; Report TR-1039472694-17; Electrical Power Research Institute: Palo Alto, CA, USA, 1996.
29. Wormleaton, P.R.; Soufiani, E. Aeration performance of triangular planform labyrinth weirs. *J. Environ. Eng.* **1998**, *124*, 709–719. [[CrossRef](#)]
30. Wormleaton, P.R.; Tsang, C.C. Aeration performance of rectangular planform labyrinth weirs. *J. Environ. Eng.* **2000**, *126*, 456–465. [[CrossRef](#)]
31. Caspersen, L.W. Fluttering fountains. *J. Sound Vib.* **1995**, *162*, 251–262. [[CrossRef](#)]
32. Naudascher, E.; Rockwell, D. *Flow Induced Vibrations. An Engineering Guide*; Dover Publications: Mineola, NY, USA, 1994; pp. 90–176.
33. Yildiz, D.; Uzupek, E. Modeling the performance of labyrinth spillways. *Int. J. Hydropower Dams* **1996**, *3*, 71–76.
34. Metropolitan Water, Sewerage and Drainage Board. *Investigations into Spillway Discharge Noise at Avon Dam*; Bulletin No. 57; ANCOLD: Sydney, NSW, Australia, 1980.
35. Indlekofer, H.; Rouvé, G. Discharge over polygonal weirs. *J. Hydraul. Div.* **1975**, *101*, 385–401. [[CrossRef](#)]
36. Osuna, A. Determinación del desagüe en un vertedor oblicuo. *Rev. Obras Públicas* **2000**, *147*, 3402.
37. Granel, C.; Toledo, M. Los aliviaderos tipo laberinto. Un nuevo enfoque para su cálculo hidráulico. In Proceedings of the II International Congress on Dam Maintenance and Rehabilitation, Zaragoza, España, 23–25 November 2010.
38. Tullis, B.P.; Young, J.C.; Chandler, M.A. Head-discharge relationships for submerged labyrinth weirs. *J. Hydraul. Eng.* **2007**, *133*, 248–254. [[CrossRef](#)]
39. Taylor, G. The Performance of Labyrinth Weirs. Ph.D. Thesis, University of Nottingham, Nottingham, UK, 1968.
40. Villemonte, J.R. Submerged weir discharge studies. *Eng. News-Rec.* **1947**, *139*, 54–56.
41. Yildiz, A.; Marti, A.I.; Gogus, M. Determination of hydraulic characteristics of flow over a triangular sectioned weir by using experimental and numerical modeling. *J. Comput. Appl. Mech.* **2021**, *52*, 215–232. [[CrossRef](#)]
42. Mattos-Villarreal, E.; Flores-Velázquez, J.; Ojeda-Bustamante, W.; Díaz-Delgado, C.; Salinas-Tapia, H. Influence of crest geometric on discharge coefficient efficiency of labyrinth weirs. *Flow Meas. Instrum.* **2021**, *81*, 102031. [[CrossRef](#)]
43. Bilhan, O.; Aydin, M.C.; Emiroglu, M.E.; Miller, C.J. Experimental and CFD analysis of circular labyrinth weirs. *J. Irrig. Drain. Eng.* **2018**, *144*, 04018007. [[CrossRef](#)]
44. Hirt, C.W.; Nichols, B.D. Volume of fluid (VOF) method for the dynamics of free boundaries. *J. Comput. Phys.* **1981**, *39*, 201–225. [[CrossRef](#)]
45. Olsen, N.R.; Nils, R.B.; Kjellesvig, H.M. Three-dimensional numerical flow modeling for estimation of spillway capacity. *J. Hydr. Res.* **1998**, *36*, 775–784. [[CrossRef](#)]
46. San Mauro, J.; Salazar, F.; Toledo, M.A.; Caballero, F.J.; Ponce-Farfán, C.; Ramos, T. Physical and numerical modeling of labyrinth weirs with polyhedral bottom. *Ing. Agua* **2016**, *20*, 127–138. [[CrossRef](#)]
47. Jiang, L.; Diao, M.; Sun, H.; Ren, Y. Numerical Modeling of Flow over a Rectangular Broad-Crested Weir with a Sloped Upstream Face. *Water* **2018**, *10*, 1663. [[CrossRef](#)]
48. Shaheed, R.; Mohammadian, A.; Gildeh, H.K. A comparison of standard k- ϵ and realizable k- ϵ turbulence models in curved and confluent channels. *Environ. Fluid Mech.* **2019**, *19*, 543–568. [[CrossRef](#)]

49. Fernández, J.M. *Técnicas numéricas en Ingeniería de Fluidos: Introducción a la Dinámica de Fluidos Computacional (CFD) por el Método de Volumen Finito*, 1st ed.; Reverté: Barcelona, España, 2012; pp. 98–294.
50. Carrillo, J.M.; Castillo, L.G. Consideraciones del mallado aplicadas al cálculo de flujos bifásicos con las técnicas de dinámica de fluidos computacional. *J. Introd. Investig. UPCT* **2011**, *4*, 33–35.
51. Celik, I.B.; Ghia, U.; Roache, P.J.; Freitas, C.J.; Coleman, H.; Raad, P.E. Procedure for estimation and reporting of uncertainty due to discretization in CFD applications. *J. Fluids Eng.-ASME* **2008**, *130*, 7. [[CrossRef](#)]
52. Roache, P.J. Perspective: A method for uniform reporting of grid refinement studies. *J. Fluids Eng.* **1994**, *116*, 405–413. [[CrossRef](#)]
53. Baker, N.; Kelly, G.; O'Sullivan, P.D. A grid convergence index study of mesh style effect on the accuracy of the numerical results for an indoor airflow profile. *Int. J. Vent.* **2020**, *19*, 300–314. [[CrossRef](#)]
54. Liu, H.L.; Liu, M.M.; Bai, Y.; Dong, L. Effects of mesh style and grid convergence on numerical simulation accuracy of centrifugal pump. *J. Cent. South Univ.* **2015**, *22*, 368–376. [[CrossRef](#)]
55. Examining Spatial (Grid) Convergence. Available online: <https://www.grc.nasa.gov/www/wind/valid/tutorial/spatconv.html> (accessed on 4 November 2021).
56. Roache, P.J. Quantification of uncertainty in computational fluid dynamics. *Ann. Rev. Fluid Mech.* **1997**, *29*, 123–160. [[CrossRef](#)]

Disclaimer/Publisher's Note: The statements, opinions and data contained in all publications are solely those of the individual author(s) and contributor(s) and not of MDPI and/or the editor(s). MDPI and/or the editor(s) disclaim responsibility for any injury to people or property resulting from any ideas, methods, instructions or products referred to in the content.